

**OPTIMIZATION OF SPECT FOR PARATHYROID
IMAGING WITH VARYING INSTRUMENTATION
PARAMETERS: A SIMULATION STUDY**

by

Ayşegül Oral

B.S., in Mathematical Engineering, Yıldız Technical University, 2013

Submitted to the Institute of Biomedical Engineering

in partial fulfillment of the requirements

for the degree of

Master of Science

in

Biomedical Engineering

Boğaziçi University

2019

**OPTIMIZATION OF SPECT FOR PARATHYROID
IMAGING WITH VARYING INSTRUMENTATION
PARAMETERS: A SIMULATION STUDY**

APPROVED BY:

Assoc. Prof. Dr. Albert Güveniř
(Thesis Advisor)

Assist. Prof. Dr. Duygu Ege

Assist. Prof. Dr. Mehmet Kocatürk

Assist. Prof. Dr. İmran Gökler

DATE OF APPROVAL: 04 January 2019

ACKNOWLEDGMENTS

I would like to thank my thesis advisor for his guidance and insightful comments during the study.

Besides my advisor, I thank my family for encouraging me throughout this work.



ACADEMIC ETHICS AND INTEGRITY STATEMENT

I, Ayşegül Oral, hereby certify that I am aware of the Academic Ethics and Integrity Policy issued by the Council of Higher Education (YÖK) and I fully acknowledge all the consequences due to its violation by plagiarism or any other way.

Name :

Signature:

Date:

ABSTRACT

OPTIMIZATION OF SPECT FOR PARATHYROID IMAGING WITH VARYING INSTRUMENTATION PARAMETERS: A SIMULATION STUDY

Parathyroid problems are frequently experienced problems. Nuclear medicine has a significant role in determining the treatment. The study tried to find out the visibility of the small adenoma with a simulation method and the usefulness of the simulation with changing optimal instrumentation and reconstruction parameters for parathyroid SPECT imaging. In previous studies, parathyroid SPECT Imaging has been optimized using physical phantoms only. In this study, an anthropomorphic phantom (Zubal Phantom) and a sphere as a parathyroid adenoma were simulated. Simulated adenoma was chosen small (0.58 cm^3). In order to create a parathyroid adenoma SPECT image, ^{99m}Tc -Sestamibi SPECT was used. SPECT acquisitions were done simulating two separate SPECT devices and different types of parallel hole collimators. It was found that the optimal parameters were LEUHR collimator, 16 iterations and no scatter correction for Siemens Symbia gamma camera (CNR:3.74). LEHR collimator, 16 iterations, without scatter correction gave better result according to the other parameters for General Electric Infinia gamma camera (CNR:2.81). Scatter correction did not result in a significant improvement in this study. The study showed that a small parathyroid adenoma could be studied with computer simulation methods. The optimal parameters could be investigated without the necessity of the machine itself. With this flexibility, optimal parameters for each camera could be studied in a shorter time in comparison with using real SPECT devices.

Keywords: Parathyroid, SPECT, Collimator, Optimization, Simulation.

ÖZET

ÇEŞİTLİ CİHAZ PARAMETRELERİ İLE PARATIROID GÖRÜNTÜLEMEDE SPECT OPTİMİZASYONU: BİR SİMÜLASYON ÇALIŞMASI

Paratiroid sorunları sık karşılaşılan sorunlardır ve tedavinin belirlenmesinde nükleer tıp önemli bir yer tutar. Bu çalışma, Monte Carlo Simülasyonu kullanarak paratiroid SPECT görüntüleme ve farklı cihaz parametrelerinin etkisini ölçme amacıyla yapılmıştır. Simüle edilen adenom küçük seçilerek sonuçlar incelenmiştir. Önceki çalışmalarda yalnızca fiziksel fantom simüle edilerek paratiroid SPECT görüntüleri optimize edilmişti. Bu çalışmada ise antropomorfik fantom (Zubal Fantom) ile simülasyon yapılmıştır. Küçük adenomların tespit edilebilmesi cerrahi operasyonlarda oldukça önemlidir. Bu çalışmada paratiroid adenomu küçük seçilip (0.58 cm^3) bir küre ile modellenmiştir. Adenomun detekt edebilmek için ^{99m}Tc -Sestamibi SPECT yöntemi kullanılmıştır. Kolimatör etkisini inceleyebilmek amacıyla, görüntüler iki ayrı SPECT cihazı ve farklı tiplerde paralel hol kolimatörler kullanılarak elde edilmiştir. Görüntüler farklı iterasyon numaraları kullanılarak rekonstrükte edilmiştir. Siemens Symbia gamma kamera için en iyi sonucu LEUHR kolimatörü, 16 iterasyon scatter correction olmadan yapılan simülasyon vermiştir (CNR:3.74). General Electric Infinia gamma kamera için ise, LEHR kolimatörü 16 iterasyon scatter correction olmadan en iyi sonuca ulaşılmıştır (CNR:2.81). Çalışma, paratiroid SPECT görüntüleme simülasyon çalışmasının doğru sonuçlar verip veremeyeceğini inceleme amacıyla gerçekleştirilmiştir. Bilgisayar simülasyon metotlarıyla, görüntüleme cihazlarına ihtiyaç kalmadan ve daha kısa sürede SPECT cihazlarının optimal parametreleri araştırılabilir.

Anahtar Sözcükler: Paratiroid, SPECT, Kolimatör, Optimizasyon, Simülasyon.

TABLE OF CONTENTS

ACKNOWLEDGMENTS	iii
ACADEMIC ETHICS AND INTEGRITY STATEMENT	iv
ABSTRACT	v
ÖZET	vi
LIST OF FIGURES	ix
LIST OF TABLES	xii
LIST OF SYMBOLS	xiv
LIST OF ABBREVIATIONS	xv
1. INTRODUCTION	1
1.1 Motivation	1
1.2 Literature Review	2
1.3 Objectives	4
1.4 Outline	5
2. BACKGROUND	7
2.1 Nuclear Medicine	7
2.1.1 SPECT Imaging	7
2.1.1.1 SPECT Instrumentation	8
2.1.1.2 SPECT acquisition	8
2.1.1.3 SPECT reconstruction	9
2.1.1.4 SPECT corrections	11
2.2 Parathyroid Scintigraphy	15
2.2.1 Parathyroid Anatomy and Physiology	15
2.2.2 Radiopharmaceuticals	16
2.2.3 Parathyroid Imaging in Nuclear Medicine	17
2.3 Monte Carlo Method in Nuclear Medicine	18
2.3.1 SIMIND	18
3. MATERIALS AND METHODS	20
3.1 Isotopes	20
3.2 Digital Phantom	20

3.3	Activity Distribution	21
3.4	Imaging System Modeling for Monte Carlo Simulation	22
3.5	Optimization Parameters	24
3.6	Data Reconstruction	27
3.7	Statistical Calculations and Analysis	27
4.	RESULTS	31
4.1	Output File Examples of the SIMIND Phantom Simulation	31
4.1.1	Siemens Symbia Gamma Camera Phantom Simulation Output File for LEUHR Collimator	31
4.1.2	General Electric Infinia Hawkeye Gamma Camera Phantom Sim- ulation Output File for LEHR Collimator	37
4.2	Reconstructed Images and Calculations	43
4.2.1	Results without Poisson Noise	43
4.2.1.1	Siemens Symbia Gamma Camera	43
4.2.1.2	General Electric Infinia Hawkeye Gamma Camera	46
4.3	Results with Poisson Noise	48
4.3.1	Poisson Noise Addition for Siemens Symbia Gamma Camera	48
4.3.2	Poisson Noise Addition for GE Infinia Hawkeye Gamma Camera	52
4.4	Summary of the Results	53
5.	DISCUSSION	56
6.	CONCLUSION	58
	REFERENCES	59

LIST OF FIGURES

Figure 1.1	The figure shows axial SPECT dual-phase delayed image that belongs to a 52 year-old man who has a parathyroid adenoma. The arrow shows the abnormality.	3
Figure 1.2	The figure was taken from the Tunninen et al.'s study. An adenoma is located in the crosshair. A) LEHR, 8 iterations, no scatter cor. B) LEHR, 16 iterations, scatter cor. C) LEUHR, 16 iterations, no scatter cor."The red arrow shows the edge artefact.	4
Figure 2.1	The main structure of an Anger (gamma) Camera.	8
Figure 2.2	OSEM reconstruction algorithm is faster than MLEM through subset property.	10
Figure 2.3	TEW Energy Spectrum.	13
Figure 2.4	The example spectra that belongs to Siemens LEHR collimator from this study. The purple dots show the total events.	14
Figure 2.5	The example spectra that belongs to Siemens LEHR collimator from this study. The green dots show the primary events.	14
Figure 2.6	Change Screenshot : Main page for input to Simind.	19
Figure 3.1	Zubal Phantom example slices displaying the thyroid.	21
Figure 3.2	A screenshot : smc2castor program is working.	27
Figure 4.1	The energy Spectra of the Siemens Symbia Gamma Camera Phantom Simulation Output File for LEUHR Collimator.	37
Figure 4.2	The energy Spectra of the GE Infinia Hawkeye Gamma Camera Phantom Simulation Output File for LEHR Collimator.	43
Figure 4.3	A. Transversal images for Siemens LEHR collimator without scatter correction B. Transversal images for Siemens LEHR collimator with scatter correction. Numbers on the left of the images are ID numbers.	44

Figure 4.4	A. Transversal images for Siemens MELP collimator without scatter correction B. Transversal images for Siemens MELP collimator with scatter correction. Numbers on the left of the images are ID numbers.	45
Figure 4.5	A. Transversal images for Siemens LEUHR collimator without scatter correction B. Transversal images for Siemens LEUHR collimator with scatter correction. Numbers on the left of the images are ID numbers.	46
Figure 4.6	A. Transversal images for GE Infinia LEHR collimator without scatter correction B. Transversal images for GE Infinia LEHR collimator with scatter correction. Numbers on the left of the images are ID numbers.	47
Figure 4.7	A. Transversal images for GE Infinia LEGP collimator without scatter correction B. Transversal images for GE Infinia LEGP collimator with scatter correction. Numbers on the left of the images are ID numbers.	48
Figure 4.8	A. Transversal images for Siemens LEHR collimator without scatter correction B. Transversal images for Siemens LEHR collimator with scatter correction. Numbers on the left of the images are ID numbers. Poisson noise was included.	49
Figure 4.9	A. Transversal images for Siemens MELP collimator without scatter correction B. Transversal images for Siemens MELP collimator with scatter correction. Numbers on the left of the images are ID numbers. Poisson noise was included.	50
Figure 4.10	A. Transversal images for Siemens LEUHR collimator without scatter correction B. Transversal images for Siemens LEUHR collimator with scatter correction. Numbers on the left of the images are ID numbers. Poisson noise was included.	51
Figure 4.11	A. Transversal images for GE LEHR collimator without scatter correction B. Transversal images for GE LEHR collimator with scatter correction. Numbers on the left of the images are ID numbers. Poisson noise was included.	52

- Figure 4.12 A. Transversal images for GE LEGP collimator without scatter correction B. Transversal images for GE LEGP collimator with scatter correction. Numbers on the left of the images are ID numbers. Poisson noise was included. 53
- Figure 4.13 A. Transversal images for Siemens LEUHR from top to bottom 8,16 and 32 iterations without scatter correction (sc) and with poisson noise (ID:13p,15p,17p) B. Transversal images for Siemens MELP from top to bottom 8,16 and 32 iterations with sc and with poisson noise (ID:8p,10p,12p). 54
- Figure 4.14 A. The best cases for GE Infinia Hawkeye Gamma Camera. Transversal images for LEHR from top to bottom 8,16 and 32 iterations without scatter correction (sc) and with poisson noise (ID:19,21,23) . B. The worst cases for GE Infinia Hawkeye Gamma Camera. Transversal images for LEGP from top to bottom 8,16 and 32 iterations with sc and with poisson noise (ID:26p,28p,30p). 54
- Figure 4.15 Tables for comparison in literature. In first table, results shows mean contrast values and in literature. 6,8,16,32 iterations with only Siemens Symbia gamma camera were examined. In second table shows mean contrast values from this study. 55

LIST OF TABLES

Table 3.1	Crystal Parameters.	23
Table 3.2	Collimator Properties for Siemens.	23
Table 3.3	Collimator Properties for General Electric Infinia.	24
Table 3.4	Parameters that are changed in the study.	24
Table 3.5	Energy Window Settings.	25
Table 3.6	The experiments and their ID numbers (TEW SC: Triple Energy Window Scatter Correction).	26
Table 4.1	Adenoma and background counts and contrast values for different parameters in Siemens LEHR collimator when Poisson Noise was not included.	44
Table 4.2	Adenoma and background counts and contrast values for different parameters in Siemens MELP collimator when Poisson Noise was not included.	45
Table 4.3	Adenoma and background counts and contrast values for different parameters in Siemens LEUHR collimator when Poisson Noise was not included.	46
Table 4.4	Adenoma and background counts and contrast values for different parameters in GE Infinia LEHR collimator when Poisson Noise was not included.	47
Table 4.5	Adenoma and background counts and contrast values for different parameters in GE Infinia LEGP collimator when Poisson Noise was not included.	48
Table 4.6	Adenoma and background counts and contrast values for different parameters in Siemens LEHR collimator when Poisson Noise was included.	49
Table 4.7	Adenoma and background counts and contrast values for different parameters in Siemens MELP collimator when Poisson Noise was included.	50

Table 4.8	Adenoma and background counts and contrast values for different parameters in Siemens LEUHR collimator when Poisson Noise was included.	51
Table 4.9	Adenoma and background counts and contrast values for different parameters in GE Infinia LEHR collimator when Poisson Noise was included.	52
Table 4.10	Adenoma and background counts and contrast values for different parameters in GE Infinia LEGP collimator when Poisson Noise was included.	53



LIST OF SYMBOLS

I_0	Transmitted photons
I	Emitted photons
μ	Linear Attenuation Coefficient
C	Contrast
CNR	Contrast to Noise Ratio
μ_M	Mean Voxel Value of the Adenoma
μ_B	Mean Voxel Value of the Background
σ_M	Standard Deviation of voxels of the adenoma
σ_B	Standard Deviation of voxels of the background
σ_{μ_B}	Standard Deviation of the Mean Voxel Value of the Background

LIST OF ABBREVIATIONS

PTH	Parathyroid Hormone
Ca	Calcium
PMT	Photomultiplier Tube
TEW	Triple Energy Window
LEHR	Low Energy High Resolution
LEUHR	Low Energy Ultra High Resolution
MELP	Medium Energy Low Penetration
LEGP	Low Energy General Purpose
SNM	The Society of Nuclear Medicine
EANM	European Association of Nuclear Medicine
PET	Positron Emission Tomography
SPECT	Single Photon Emission Computed Tomography
US	Ultrasonography
EM	Expectation Maximization
MLEM	Maximum Likelihood Expectation Maximization
OSEM	Ordered Subset Expectation Maximization
CNR	Contrast to Noise Ratio

1. INTRODUCTION

1.1 Motivation

In recent years, certain diagnostic imaging techniques give information about physical characteristics of a tissue or an organ. In addition to that, molecular imaging techniques have come into prominence because of their benefits in the visualization of the target's biological functions. These techniques provide a unique estimation for personalized patient care. One of the applications of these techniques is in parathyroid imaging.

A parathyroid adenoma is a benign tumor and it generally appears on one of the glands. Normally, every parathyroid gland is approximately 5 to 7 mm and too small to be seen [1]. When a parathyroid disease appears these glands get bigger. These abnormal glands could not be identified without imaging methods such as ultrasonography or scintigraphy [1]. The benign parathyroid tumor release Parathyroid hormone (hyperparathyroidism) more than the body need. In general, the cause is not known. Unless the adenoma is removed, everybody who has an adenoma will eventually have an osteoporosis and the risk of developing other cancers will increase because of the abnormal Ca levels. On the other hand, parathyroid glands can be found anywhere from the base of the tongue, down through the neck, and even into the upper part of the chest [2]. As a result of this location variety [3], finding the correct place of the parathyroid is hard. Nuclear Medicine techniques are very useful to localize the adenoma.

The main reason for the primary hyperparathyroidism is a parathyroid adenoma[4]. Surgery is the most common way to treat the parathyroid disease (hyperparathyroidism). There are no medications that work to cure parathyroid problems, therefore a surgical therapy is necessary for removing the adenoma in general [5]. However, parathyroid glands have the most unpredictable location in body [2].

In a standard parathyroid operation, the surgeon has to detect all neck and four parathyroid glands and take whichever one(s) has a problem. Recent developments ensure removing enlarged parathyroid adenomas with a minimally invasive parathyroidectomy. This method reduces surgical problems because the area of the intervention gets smaller with this procedure. Benefits of minimizing the surgical intervention area are less surgical complications, better esthetic consequence, shorter healing time and hospitalization, better results for potential further operations in that region [6]. Therefore, localize the adenoma is highly recommended before the operation to define true surgical procedure [7]. Before a surgical operation, these localization studies are increasingly becoming the standard of care nuclear imaging as a SPECT. These scans enhance diagnostic accuracy and assist in anatomical localization.

To conduct interventions, exact preoperative imaging is necessary, showing the exact place of abnormal glands [6]. Detecting abnormalities as early as possible is significant for efficient surgical processes. It may be difficult to localize small parathyroid abnormalities with SPECT because of high noise levels and low spatial resolution [8]. The collimator has a significant role for sensitivity and resolution in SPECT, therefore it makes a difference to detection of an adenoma [9].

1.2 Literature Review

In recent years, parathyroid SPECT imaging studies have been done using dual phase ^{99m}Tc -Sestamibi or simultaneous ^{99m}Tc -Sestamibi/ ^{123}I subtraction SPECT protocols in general. But dual phase ^{99m}Tc -Sestamibi is mostly used (as in figure 1.1) for localize the adenoma [10] in the recent articles [11, 12, 13, 14, 15]. The dose range of the studies is between 340 and 1110 MBq.

According to Martinez et al.'s study, ^{99m}Tc -Sestamibi dual-phase imaging protocol was used in order to image abnormal parathyroid tissue. Three cases were examined. Results showed that 2 to 3 hours after administered ^{99m}Tc -Sestamibi (delayed phase), the radioactivity only seems in abnormal parathyroid glands [16].

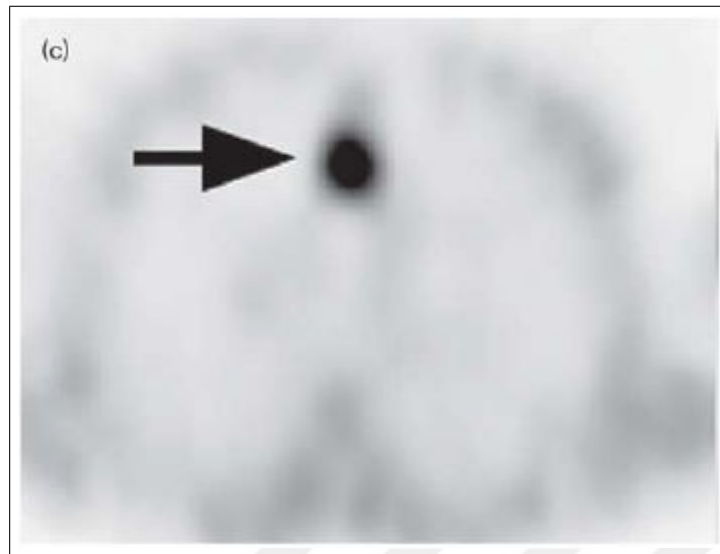


Figure 1.1 The figure shows axial SPECT dual-phase delayed image that belongs to a 52 year-old man who has a parathyroid adenoma. The arrow shows the abnormality.

Nichols et al. studied the impact of reconstruction algorithms for ^{99m}Tc -Sestamibi SPECT/CT parathyroid. Two reconstruction algorithms were used (Filtered back projection and iterative reconstruction method) and compared [17].

Tunninen et al. investigated an adenoma contrast with ^{99m}Tc -Sestamibi/ ^{123}I subtraction SPECT/CT protocol. Multiple parameters were chosen such as collimator, energy window settings and different reconstruction parameters in order to optimize parathyroid scintigraphy [7].

Mallak et al. tried to optimize find the small adenomas. Their results show that dual tracer MIBI/ TcO_4 provides better results planar imaging for detection of small adenomas [18].

Tunninen et al. compared the properties of LEHR, LEUHR and MELP collimators for simultaneous dual isotope imaging. To identify small lesions with MELP is difficult because of the low resolution. LEUHR looks better for ^{99m}Tc as could be seen in figure 1.2, but LEUHR and LEHR need to be tested in septal penetration. The study showed that testing before practice is significant in order to identify the collimator limitations [19].

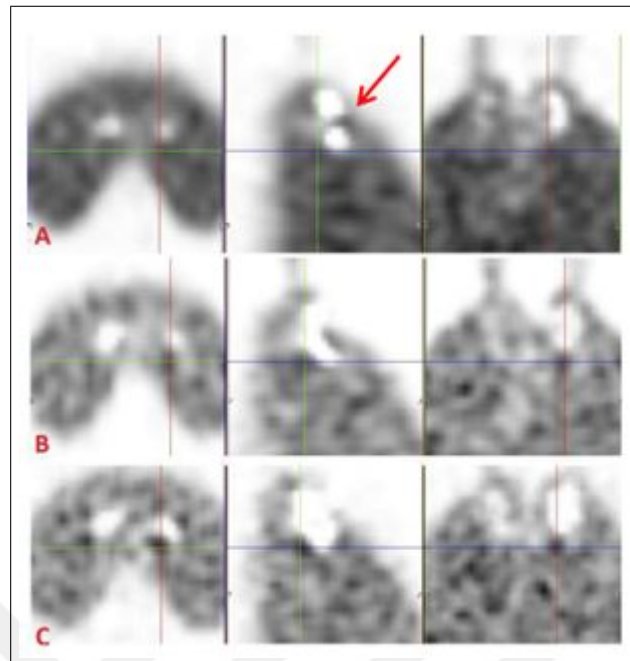


Figure 1.2 The figure was taken from the Tunninen et al.'s study. An adenoma is located in the crosshair. A) LEHR, 8 iterations, no scatter cor. B) LEHR, 16 iterations, scatter cor. C) LEUHR, 16 iterations, no scatter cor."The red arrow shows the edge artefact.

According to the Reeve et al.'s study minimally invasive parathyroidectomy has to turn into a worldwide surgical application. A minor cut is enough for the operation and results to show that minimally invasive technique has used for 20 years [5].

Tunninen et al. performed 5 different protocols and investigated the similarities. Parallel hole and pinhole collimator, planar and SPECT images have been tested and acquisition time has been another parameter. The study also shows that the main variable affecting detection of parathyroid adenoma is its size [20].

1.3 Objectives

Mainly, the aim of this study is to carry out parathyroid SPECT using Monte Carlo Simulation and to study the effect of instrumentation parameters (different scanners) [7]. The study will try to find out a more accurate definition of abnormalities with SPECT. Advance image quality will ensure better diagnostic values for specific

adenoma.

The performance of SPECT in small lesions is not efficient and optimization is needed. The collimator has a significant role for sensitivity and resolution in SPECT, therefore it makes a difference to detection of an adenoma [9].

In previous studies, parathyroid SPECT Imaging has been optimized using physical phantoms only. This study used Monte Carlo Simulation for the first time to our knowledge. The advantage of the simulation studies is that changing parameters and examining the effect of parameters are easier and less costly. The study tried to investigate the sensitivity of the optimal values to change instrumentations. The optimum parameters may change from device to device. This needs to be checked for various brands of SPECT devices. With physical devices and phantoms, this process is time-consuming. Through this simulation method, optimal parameters for different types of equipment could be studied by changing instrumentation parameters. Through this flexibility of the simulation studies, optimal parameters for various devices for SPECT could be performed less costly.

1.4 Outline

Chapter 1 gives information about motivation, literature about the study and objectives.

Chapter 2 mentions the subject's background. Power and fundamentals of Nuclear Medicine and SPECT imaging are explained in general. Parathyroid scintigraphy is described. This chapter also presents information about the Monte Carlo Method and SIMIND Monte Carlo program.

Chapter 3 explains the methodology of the study.

Chapter 4 gives the results.

Chapter 5 and 6 discuss and conclude the study respectively.



2. BACKGROUND

2.1 Nuclear Medicine

In recent years, one of the most significant development is studies in the personalized medicine area. Personalized medicine has the main role in order to provide exact patient therapy. Molecular Imaging techniques provide unique estimation for personalized patient care, therefore has gained importance. The techniques not only gives information about physical characteristics of a target but also visualizes a target's biological functions non-invasively [21].

In Nuclear Medicine Imaging, certain radioactive materials are attached to a pharmaceutical compound. That is called radiopharmaceutical. After transportation of the radiopharmaceuticals in a body, radioactive decays appear. As a result of the decays, gamma rays or high energy photons appear and a special gamma-ray camera could recognize these rays or photons. Then they form an image according to their intensity [22]. Together with the introduction of new radiopharmaceuticals, probable investigations have risen [8].

Nuclear Medicine Imaging is mainly used in diagnosis or therapy of a disease.

2.1.1 SPECT Imaging

One of the most common technique of nuclear medicine imaging is Single Photon Emission Computed Tomography. In SPECT, according to the distribution of the radioactive molecules, three-dimensional images are created due to different directions recording. These 3D images could define the precise properties of the problem [23].

It was firstly designed by Kuhl and Edwards in 1963 [24], and there have been a

lot of innovations like a combination of SPECT and CT systems now. It is commonly available (with respect to PET) and offers a wide range of studies with a variety of radiopharmaceuticals.

2.1.1.1 SPECT Instrumentation.

SPECT uses a gamma camera which detects gamma rays emitted by certain radiopharmaceuticals. Every decay emits a gamma ray in random ways from the source and a collimator ensures choose the photons that only coming through. Rays passing from the collimator are detected by photomultiplier tubes and tubes generates electrical signal that is proportional with the amount of ray that hits each tube, then pulse height analyzer chooses only specific energy window for monitor and image matrix is formed [23].

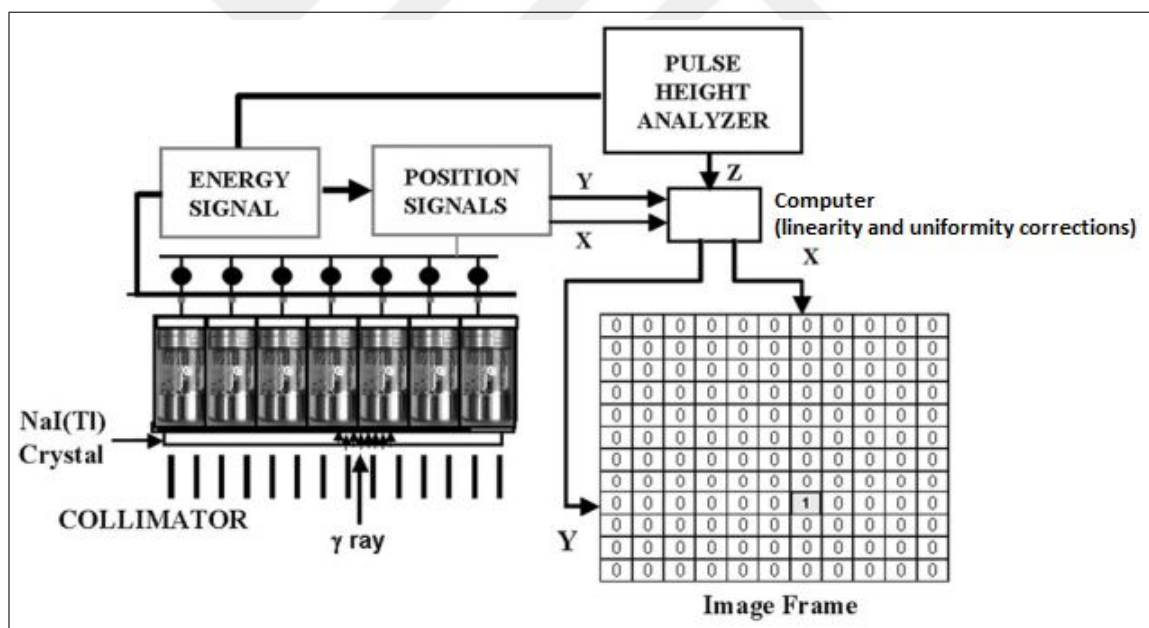


Figure 2.1 The main structure of an Anger (gamma) Camera.

2.1.1.2 SPECT acquisition.

Each measured signal is sampled in time and space and all SPECT systems use these discrete samples [8]. Step and shoot, continuous step and shoot and continuous methods are used for SPECT acquisitions [25]. Step and shoot approach is commonly

used in order to measure the signals. In this approach, the camera rotates around the subject and shoots in small predetermined periods.

2.1.1.3 SPECT reconstruction.

In order to analyze tomographic slices of a source certain reconstruction algorithms are applied in nuclear imaging [26]. These algorithms heavily change the visualization of the objects.

Analytical methods (e.g. Filtered back projection) do not always give good results especially for noisy images, therefore according to the most researchers, iterative algorithms are used more than analytical methods for SPECT reconstruction [23, 26]. The most important benefit of the iterative method is that resolution, attenuation, penetration and scattered of gamma photons could be modeled [23], these properties are needed to true correction. Iterative methods are more complex and slower than analytical methods. They rely on the initial image estimation.

A big improvement of the iterative method is the expectation maximization (EM) algorithm that is preferred in computational probabilistic studies [27]. In the 1980s, statistical based Maximum Likelihood Expectation Maximization (MLEM) algorithm is firstly used in Positron Emission Tomography (PET) [28]. MLEM algorithm is accepted on the basis iterative reconstruction algorithm. In order to reconstruct the images faster, Ordered Subset Expectation Maximization (OSEM) has been created (Figure 2.2). Such iterative reconstruction methods are appropriate for nuclear medicine studies (PET and SPECT) because of the small reconstruction volumes. They ensure lower noisy images than analytic reconstruction techniques such as Filtered back projection (FBP). FBP has been generally used in Computed Tomography.

In iterative reconstruction algorithms, as iteration number increase, better contrast values appear but as opposed to this, image noise also increases. As a result, a high number of iterations is not always the case and keeping the balance of the parameters determine the choice of the iteration number in reconstruction parts [28].

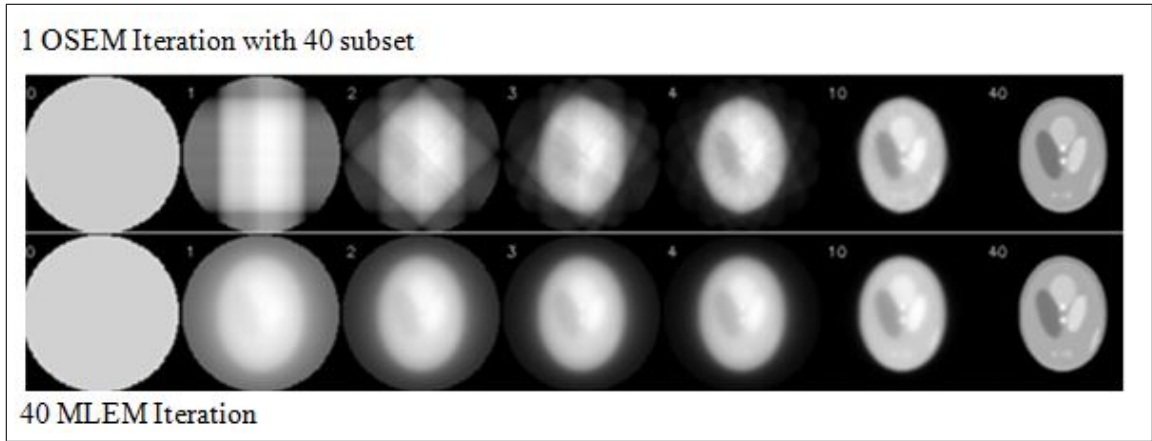


Figure 2.2 OSEM reconstruction algorithm is faster than MLEM through subset property.

When performing MLEM or OSEM approach, several complex calculations are carried out. In Eq. 2.1, H represents the imaging system modelling [29].

$$\bar{p}_i = \sum_{j=1}^N H_{ij} f_j \quad (2.1)$$

where H_{ij} shows the likelihood emission of j^{th} voxel in i^{th} projection, f_j represents j^{th} voxel activity and \hat{p}_i is the mean of the i^{th} projection [29].

MLEM approach has an iterative equation as Eq. 2.2. $\hat{f}^{(0)}$ represents primary image estimate.

$$f_j^{(n+1)} = \frac{\hat{f}_j^{(n)}}{\sum_{i'} H_{i'j}} \sum_i H_{ij} \frac{p_i}{\sum_k H_{ik} \hat{f}_k^{(n)}} \quad (2.2)$$

where $\hat{f}^{(n)}$ is the present guess and $\hat{f}_j^{(n+1)}$ is the next guess of j^{th} voxel. The iterations are being repeated until reach the maximum likelihood solution.

A little replacement on the MLEM reconstruction formula gives OSEM reconstruction approach. In Eq. 2.3, the total subset number is B (when there is 8 subset, B=8) and that means OSEM approach is B times faster than MLEM [29]. Here, the back projection steps only divided by the projections in subset S_b . When total subset number is 1, OSEM returns to MLEM algorithm.

$$f_j^{(n+1)} = \frac{\hat{f}_j^{(n)}}{\sum_{i' \in S_b} H_{i'j}} \sum_{i' \in S_b} H_{ij} \frac{p_i}{\sum_k H_{ik} \hat{f}_k^{(n)}} \quad (2.3)$$

2.1.1.4 SPECT corrections.

Within a given source, quantifying the true radioactivity concentration process is spoiled by attenuated and scattered photons, septal penetration and partial volume effects. In order to obtain the nearest image approximation, certain corrections must be done in projection images' reconstruction processes [8].

Attenuation Correction

Attenuation is the loss of true counts because of the photon absorption in the body or by scattering out of the detector field of view [30]. Loss of true events due to attenuation raises artifacts and noise. The amount of attenuation is related to material's or tissue's electron density and path length. It could be calculated as Eq. 2.4.

$$I = I_0 \cdot \exp\left(-\int_0^s \mu(x, y) ds\right) \quad (2.4)$$

where I_0 represents transmission photons, I represents emission photons with $\mu(x, y)$ as the linear attenuation coefficient for two-dimensional model.

The aim is to decrease the impact of attenuation in order to provide a valid representation of images that are more uniform and allow for higher confidence.

Septal Penetration Correction

When a gamma ray that has higher energy from the chosen energy level for image formation moves through the collimator, septal penetration may happen. Moving one collimator hole to another one is not a desirable event for SPECT. These rays should not contribute to the image because image contrast and accuracy will decrease [8]. While designing a collimator small septal penetration level must be the first important criterion. In order to ensure that determining proper septal thickness is required.

Deconvolution is one of the techniques for penetration correction. It works to fix a blurred image to unblurred by using point spread function [31]. In order to carry out the deconvolution method, system's response to a point source must be known.

On the other hand, triple energy window correction that is used for scatter correction is also used to reduce septal penetration artifacts. Because these artifacts are observed in scatter window data [31].

Scatter Correction

In SPECT, a scattered gamma ray may either be absorbed by the patient or go through the surrounding places. The recorded scattered gamma rays will give wrong data about its origin and direction, consequently cause uncertainties. Contrast also will decrease because of the uncertainties.

In this study, triple energy window scatter correction (TEW) technique was included when operating the images. In order to measure approximate scattered photons, two neighboring lower and upper windows are chosen in each side of the photopeak window. These acquired subwindows are supposed the main window's scattered photons.

Eq. 2.5 is calculated for each pixel.

$$C_{TEWscatter} \simeq \left(\frac{C_{left}}{W_s} + \frac{C_{right}}{W_s} \right) \cdot \frac{W_m}{2} \quad (2.5)$$

where, W_m and W_s represent photopeak window width and right/left scatter windows' width (keV) respectively. C_{left} and C_{right} represent counts in left and right window [32].

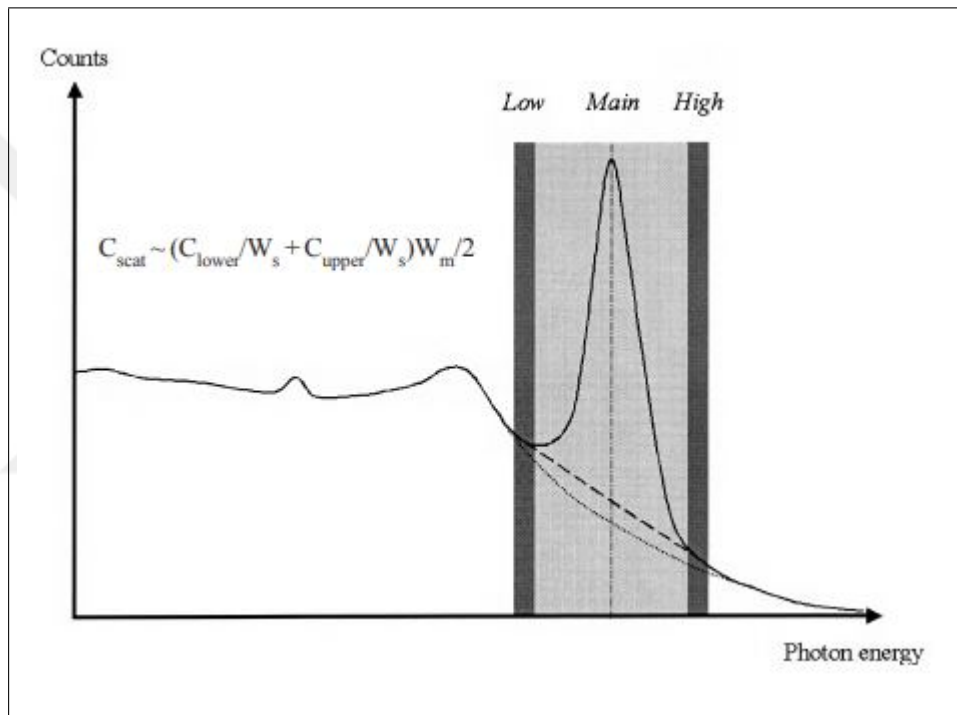


Figure 2.3 TEW Energy Spectrum.

After scatter photons are calculated, they are subtracted from the main window [33]. The primary photons' counts could be calculated for each pixel as Eq. 2.6;

$$C_{primary} = C_{total} - C_{TEWscatter} \quad (2.6)$$

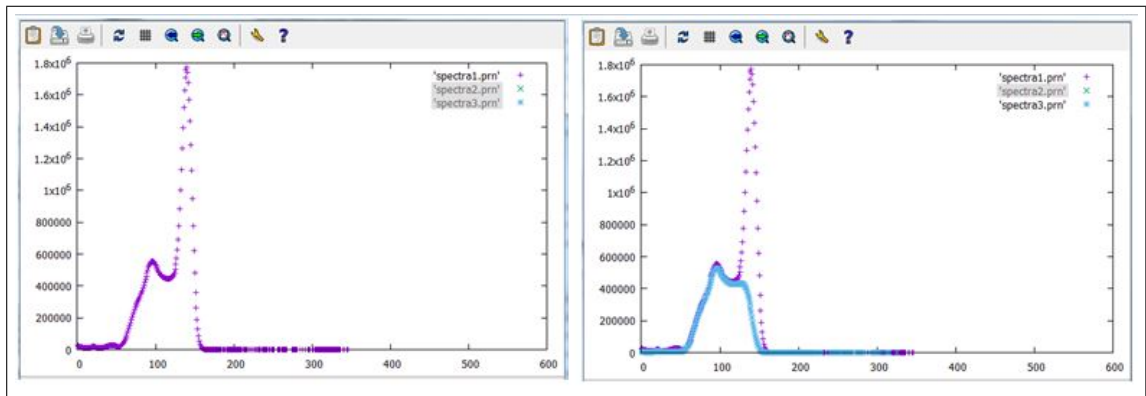


Figure 2.4 The example spectra that belongs to Siemens LEHR collimator from this study. The purple dots show the total events.

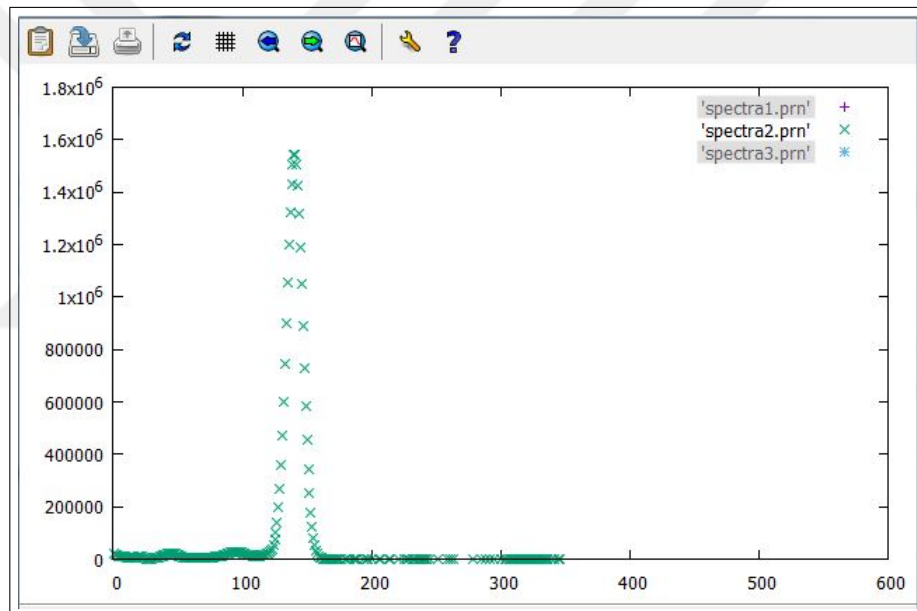


Figure 2.5 The example spectra that belongs to Siemens LEHR collimator from this study. The green dots show the primary events.

Partial Volume Correction

When working in small areas or tumors, because of the restricted sampling and poor resolution of SPECT imaging system certain activities are lost and could not be calculated the activity concentration accurately in this small region. A blur appears in consequence of the poor resolution, thus some activities go surrounding pixels. This event is known partial volume effect and disrupts the real outcome.

In order to avoid partial volume effect for this study, every side of the chosen adenoma pixels for calculations has an activity. That means the adenoma comprises the whole of the chosen pixels.

2.2 Parathyroid Scintigraphy

The great number of parathyroid problems are because of a single adenoma. Scintigraphy could identify adenomas that have more than 500 mg. Less than 500 mg could be found with fewer sensitivity [34]. In order to acquire an image, a dual phase method or a subtraction method (two radiopharmaceuticals required) is used. An average recommended total acquisition time is 25 minutes (over a 180 arc at least 60 projections is ideal) and an acquired image matrix should be at least 128x128. For the reconstruction 10 subset and 2 iterations or more are recommended [34].

2.2.1 Parathyroid Anatomy and Physiology

In a human body, just parathyroid that works in hormone metabolism has four in number in general, but more than 4 glands could also be seen [35]. Parathyroid glands form at the base of the tongue in early embryogenesis. The third pharyngeal pouch forms the thymus and fourth pharyngeal pouch also forms the thyroid tissue, parathyroids comes from these pouches [35]. Typically the glands go down into their normal locations together with thyroid and thymus but during the migration process occasionally the glands could stick and as a consequence especially lower glands could be identified from the base of the tongue to upper chest [35]. Because of the variety of possible locations, it is difficult to find the exact positions of them in surgical operations.

Parathyroid glands balance Calcium level that is one of the most important elements for many systems such as muscle function, nerve conduction or digestive system, by producing parathyroid hormone (PTH). It is directly effective on bones and kidneys with has indirect impacts on intestinal systems through vitamin D processes.

It also stimulates reabsorption of calcium from the kidney and conversion of vitamin D3 to its effective version. The surface of the parathyroid cells has a calcium-sensing receptor that balance Calcium in the blood. The normal constant level of Calcium is 8.5-10.2 mg/dl [36], other levels disrupt the body.

A parathyroid adenoma, that is a benign tumor on one of the parathyroid glands, causes the affected gland to release excessive Parathyroid Hormone (PTH) which is known hyperparathyroidism. Only in rare cases, more than one of the parathyroid glands grows into a tumor. Unless the abnormal tissue is removed, the patient will eventually have an osteoporosis and the risk of developing other cancers will increase because of the abnormal Calcium levels. Nuclear Medicine techniques give successful results in order to localize the adenoma.

2.2.2 Radiopharmaceuticals

There are four types of radiopharmaceuticals that are used in parathyroid scintigraphy.

^{99m}Tc -Sestamibi (1-isocyano-2-methoxy-2-methylpropane) is largely in the cells that have a large number of mitochondria and metabolic activity. On the other hand, specific abnormal tissues also wash out it. ^{99m}Tc -Sestamibi is taken from both parathyroid and thyroid tissue, however abnormal parathyroid tissue washes out it slower in general. The suggested activity range is 740-1110 MBq for adults [34]. It has 6 hours physical half-life and 140 keV photon energy.

^{99m}Tc -tetrofosmin is taken from both parathyroid and thyroid tissue with the same washout, but it could be used for a dual-isotope subtraction method [34].

^{99m}Tc -pertechnetate determines the thyroid tissue bounds, therefore with the subtraction method (with ^{99m}Tc -Sestamibi) only a parathyroid adenoma image appears. The suggested activity range is 74-370 MBq [34].

^{123}I is used to specify the thyroid tissue bounds and used with ^{99m}Tc -Sestamibi in subtraction method for parathyroid scintigraphy. This subtraction process is done only for the disappearance of the thyroid [34]. It has 159 keV photon energy and 13 hours biological half-life. Recommended activity range is 7.5-22 MBq [34].

2.2.3 Parathyroid Imaging in Nuclear Medicine

There are different methods that have been performed clinically for an abnormal parathyroid localization. Invasive methods are not always wanted to carry out because of the technical difficulties and risks [37]. Therefore, non-invasive techniques are ideal for many cases but they have some drawbacks. Morphological techniques such as magnetic resonance have high contrast and image resolution but poor accuracy and differentiation the tissues [38]. The other non-invasive technique is scintigraphy.

There are basically two types of imaging modalities that are mostly used in parathyroid scintigraphy in nuclear medicine. In planar scintigraphy, only a single two-dimensional image is acquired for finding the distribution of the gamma rays. It is similar to a planar X-ray scan, the difference is that it uses emitted gamma rays from the patient. It only gets photons in one direction and uses an Anger camera. In SPECT, a series of two-dimensional images are obtained from various angles, through these series of images, the projection data is created. It uses Anger camera, too.

According to Slater et al.'s and Moka et al.'s studies, SPECT imaging improves the probability of finding the parathyroid adenoma accurately by the side of planar imaging for dual-phase Sestamibi protocol [39, 40]. ^{99m}Tc Sestamibi SPECT studies have higher sensitivity in comparison to planar imaging in literature [41].

The choice of the collimator that may have an influence the sensitivity, resolution and noise of the scan are critical for SPECT Imaging [42]. It has a role of determining the correct localization of the emitted photons that come from the patient's body. Collimator types are divided into two categories as pinhole and multi-pinhole

collimators.

Parathyroid adenomas are generally very small. These adenomas can be expanded by being used pinhole collimators. Pinhole collimators ensure the highest resolution and sensitivity in comparison to the other types [38], but it only allows viewing small areas. On the other hand, under the title of multi-pinhole collimators, parallel hole collimators could be used for parathyroid imaging. In this type, the area from the upper neck to the lower chest could be seen [38].

According to the last Finnish hospitals' survey, only 28% of the parathyroid imaging has been performed by pinhole collimators [43].

2.3 Monte Carlo Method in Nuclear Medicine

Monte Carlo Method is a simulation procedure that uses randomly generated numbers. In nuclear medicine, certain parameters almost impossible to measure because of the randomness such as statistics over radiation interaction parameters in certain objects and attenuation coefficients for each photon path [44], therefore Monte Carlo Method is a useful tool to advance medical instrumentations and optimize analysis of the image data. The main working principle of Monte Carlo is making a random selection from system's probability density functions [44].

2.3.1 SIMIND

In the area of Nuclear Medicine imaging many Monte Carlo programs are ready and accessible in the public domain. SIMIND is one of these beneficial programs that simulates SPECT gamma camera. In short, it has two major programs, CHANGE program in order to modify the parameters and SIMIND program in order to operate simulation (that reads the input parameters). Simulated decay radiate gamma photons and these photons follow up in every section towards the gamma camera. With SIMIND

change Program, many parameters such as scintillation camera parameters, phantom parameters, collimator parameters, simulation parameters or image parameters could be changed easily. SIMIND 's Change screenshot could be seen as an example in Figure 2.6.

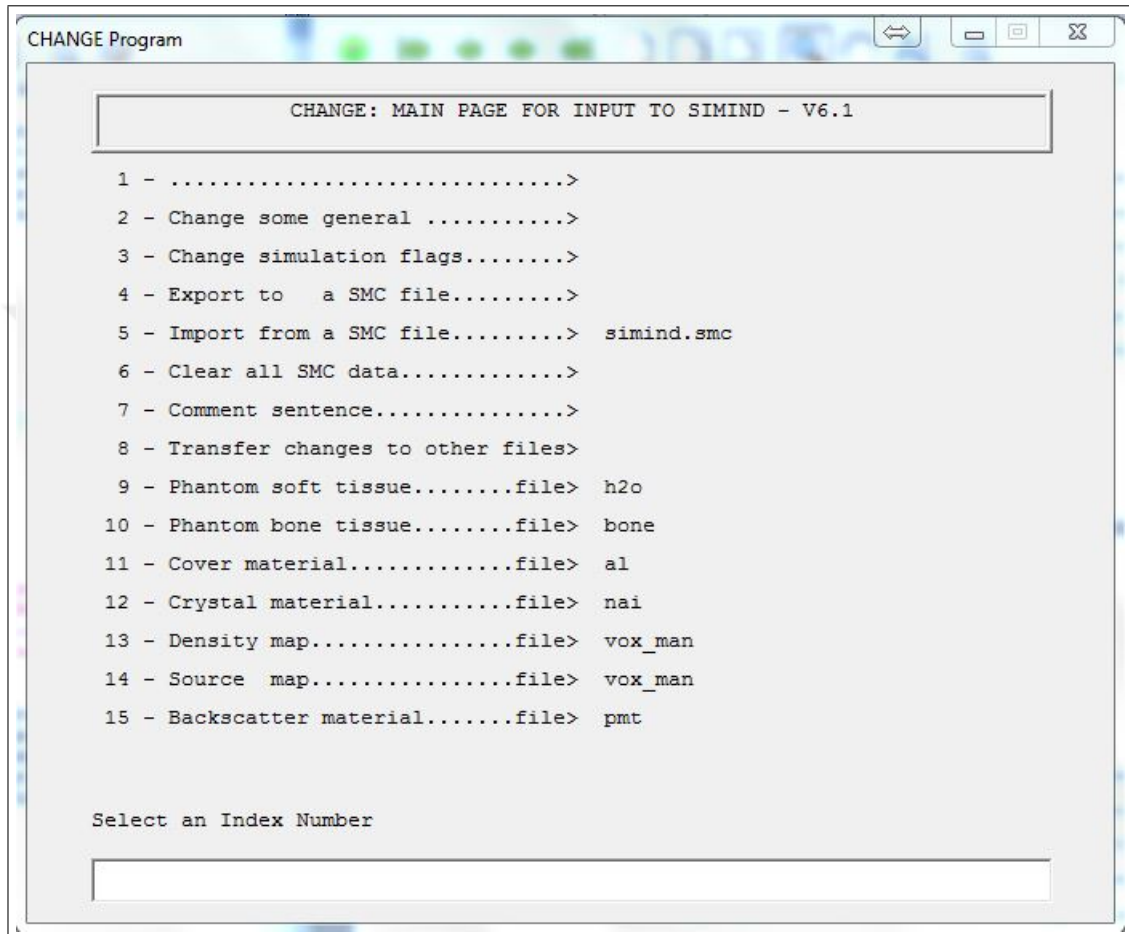


Figure 2.6 Change Screenshot : Main page for input to Simind.

3. MATERIALS AND METHODS

In order to carry out this simulation study, Simind Monte Carlo Simulation program was used. The research was performed by simulating two different devices (Siemens Symbia Intevo Gamma Camera and General Electric Infinia Hawkeye Gamma Camera).

3.1 Isotopes

Different image acquisition protocols for parathyroid imaging were described in section 2.2.2 . Dual-phase ^{99m}Tc - Sestamibi or subtraction technique is the most commonly applied for parathyroid scintigraphy [39]. Sestamibi is held not only parathyroid but also thyroid tissue. But parathyroid washes out it slower, thus detection is possible by delayed phase [39]. This work has concentrated on a ^{99m}Tc -Sestamibi single isotope (delayed imaging) protocol.

3.2 Digital Phantom

In order to carry out the closest simulation to the real human anatomy, certain anthropomorphic phantoms were performed [45]. Zubal voxel-based phantom is one of these phantoms that supported in SIMIND software. It is modeled from a series of sliced of living human bodies. Several Zubal phantom versions were created according to the interested area in the whole body. In this study body torso phantom with no arms or legs attached was used. The slice resolution was chosen 128x128 pixels [7, 34] and 243 slices as the Zubal phantom 's original structure.

The examples of Zubal Phantom slices could be seen in Figure 3.1.

SIMIND was programmed to create spherical tumors creating from the center of

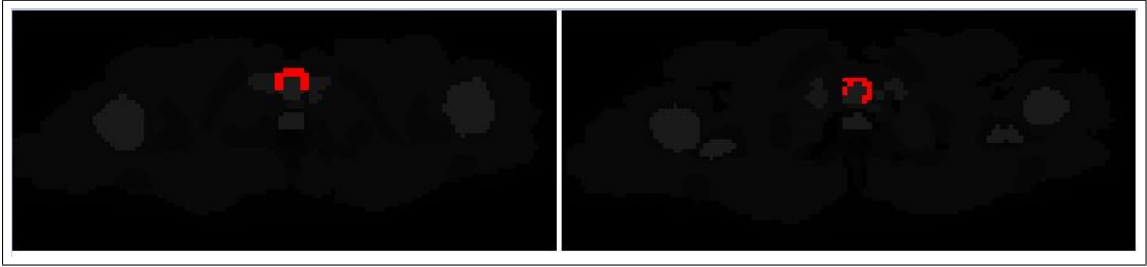


Figure 3.1 Zubal Phantom example slices displaying the thyroid.

the center pixel. Pixel size and slice thickness were defined 0.24 cm per pixel in the x, y and z plane with CHANGE program. According to the study, parathyroid adenoma was simulated as a small sphere and it was placed behind the thyroid gland [7]. In x, y and z direction, 3x3x3 pixel was fully selected for adenoma dimensions according to the SIMIND lesion creation properties. According to this the adenoma's radius was selected 0.52 cm [7].

3.3 Activity Distribution

The total source activity (in MBq) could be defined with index 25 in the Simind change program. This value reflects total activity times the per projection acquisition time (because the corresponding acquisition time is 1 second in SIMIND default) [46].

In order to find the total source activity, total voxel-based anthropomorphic Zubal phantom volume was calculated. According to Zubal torso phantom data, total voxel number is 996021 and 1 voxel volume was chosen 0.013 cc (0.24 cm x 0.24 cm x 0.24 cm). As a consequence, the total phantom volume is found 13768 cc (996021 x 0.013). In order to carry out a similar study to the last studies [7], approximately 0.03 MBq/cc was used (In Tunninen et al.'s study, physical torso phantom that has 11743 ml volume was used and filled with 350 MBq of ^{99m}Tc . That means 0.03 MBq/ml.). Thus 413 MBq (it is consistent with SNM and EANM guidelines [34, 35]), 13768 cc multiplied by 0.03 MBq/cc, was given into torso as a total source activity.

In this study, acquisition time is 33 seconds per projection [7] therefore total source activity must be multiplied with 33 from the definition of the index 25 that equals to 13629 MBq. Distribution of the activity was assumed to show a uniform spread for all organs [7]. In order to ensure a uniform distribution, the .zub file in SIMIND was redefined [46].

On the other hand, parathyroid adenoma was modeled as a sphere behind the thyroid gland and filled ^{99m}Tc with a density of 0.5 MBq/cc [7]. ^{99m}Tc concentration ratio was chosen at approximately 16:1 for the parathyroid adenoma and background models [7].

3.4 Imaging System Modeling for Monte Carlo Simulation

In order to do Monte Carlo Simulation SIMIND Software Program was used. The main simulation parameters can be found below.

Photon Energy (keV)	: 140.000
Half-length Source (cm)	: 30
Half-length Phantom (cm)	: 30
Height to Detector Surface (cm)	: 31(from the center of phantom)
Phantom Type	: -2
Source Type	: -2
Upper Window Threshold (keV)	: 147
Lower Window Threshold (keV)	: 133
Energy Resolution (140 keV) %	: 9.9
Intrinsic Resolution (140 keV)(cm)	: 0.3
Source Activity (MBq)	: 13631.000
Image Matrix Size	: 128 x 128
Number of SPECT Projections	: 48
SPECT Rotation (3 = 180)	: 3

Pixel Size (cm) : 0.24
 Code Definitions in Zubal Phantom : 1

Table 3.1
 Crystal Parameters.

Parameters	Siemens	General Electric
Crystal Half-length/Radius (cm)	29.55	27
Crystal Thickness (cm)	0.95	0.95
Crystal Half-width (cm)	22	20

Crystal parameters could change from device to device. In this study, two separate instruments were simulated in order to perform the effect of instrumentation parameters. The parameters in Table 3.1 were taken from the specifications documents [47, 48]. Both are equipped with parallel-hole collimators [7]. There are also collimator parameters that could be changed in Simind Change program. Firstly, Siemens Symbia Low Energy High Resolution (LEHR), Low Energy Ultra High Resolution (LEUHR), and Medium Energy Low Penetration (MELP) collimators were simulated. Secondly, General Electric Infinia Hawkeye Low Energy High Resolution (LEHR) and Low Energy General Purpose (LEGP) collimators were chosen to be simulated. Their certain important specifications were referred in Table 3.2 and Table 3.3.

Table 3.2
 Collimator Properties for Siemens.

COLLIMATOR	LEHR	LEUHR	MELP
Hole Shape	Hex	Hex	Hex
Number of Holes	148000	146000	14000
Hole Length	24.05 mm	35.08 mm	40.64 mm
Septal Thickness	0.16 mm	0.13 mm	1.14 mm
Hole Diameter	1.11 mm	1.16 mm	2.94 mm
Sensitivity (cpm/ μCi) (100 mm)	202 (^{99m}Tc)	100 (^{99m}Tc)	275 (^{99m}Tc)
System Resolution (100 mm)	7.5 mm	6.0 mm	12.5 mm
Septal Penetration	%1.5	%0.8	%1.2

Table 3.3
Collimator Properties for General Electric Infinia.

COLLIMATOR	LEHR	LEGP
Recommended Isotope	Tl-201 / ^{99m} Tc Studies	Tl-201 / ^{99m} Tc Studies
Hole Shape	Hex	Hex
Number of Holes	86300	56560
Hole Length	35 mm	35 mm
Septal Thickness	0.2 mm	0.2 mm
Hole Diameter	1.5 mm	1.9 mm
Sensitivity (cpm/ μ Ci) (100 mm)	160(^{99m} Tc)	270(^{99m} Tc)
System Resolution (100 mm)	7.4	9
Septal Penetration	%0.3	%0.8

3.5 Optimization Parameters

SPECT imaging parameters could be divided into three main categories as device, acquisition, and processing parameters. The effect of collimator types, various camera brands, and crystal thickness could be studied under the title of device parameters. Acquisition parameters include attenuation correction, scatter correction, number of projections, projection time, and penetration. Processing parameters comprise like a number of iterations and Number of Subsets. All could be expanded.

Parameters that were changed in this study were referred to in Table 3.4.

Table 3.4
Parameters that are changed in the study.

DEVICE	ACQUISITION	PROCESSING
Collimator Type	With/Without Scatter Correction	Number of Iterations

According to these parameters, the design of the experiments could be seen in Table 3.6. Same parameters were used for the second brand with LEHR and LEGP collimators.

In this study, every simulation case has an attenuation correction and penetration properties. 15% window width of the photopeak was chosen for each side of the photopeak.

Table 3.5
Energy Window Settings.

Energy Window	Photopeak at	Window Width	Window Limits (keV)
Scatter - Left	-	%15	112 - 133
Scatter - Right	-	%15	147 - 168
^{99m}Tc	140 keV	%10	133 - 147

Table 3.6

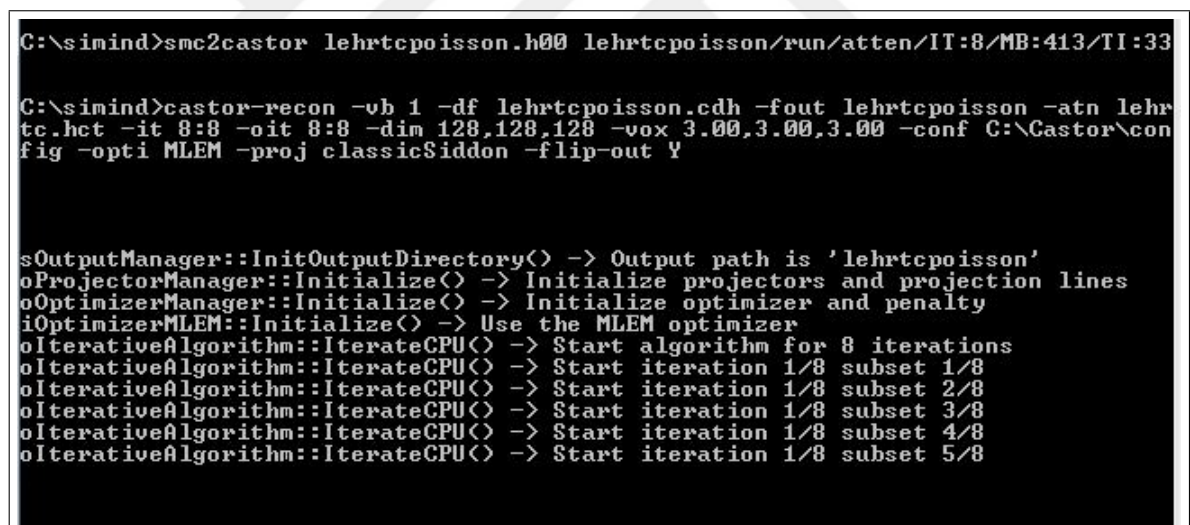
The experiments and their ID numbers (TEW SC: Triple Energy Window Scatter Correction).

EXP. NO	TRACER	COLLIMATOR	IT. NO	SUBSET NO	TEW SC
1	^{99m}Tc	Siemens LEHR	8	8	No
2	^{99m}Tc	Siemens LEHR	8	8	Included
3	^{99m}Tc	Siemens LEHR	16	8	No
4	^{99m}Tc	Siemens LEHR	16	8	Included
5	^{99m}Tc	Siemens LEHR	32	8	No
6	^{99m}Tc	Siemens LEHR	32	8	Included
7	^{99m}Tc	Siemens MELP	8	8	No
8	^{99m}Tc	Siemens MELP	8	8	Included
9	^{99m}Tc	Siemens MELP	16	8	No
10	^{99m}Tc	Siemens MELP	16	8	Included
11	^{99m}Tc	Siemens MELP	32	8	No
12	^{99m}Tc	Siemens MELP	32	8	Included
13	^{99m}Tc	Siemens LEUHR	8	8	No
14	^{99m}Tc	Siemens LEUHR	8	8	Included
15	^{99m}Tc	Siemens LEUHR	16	8	No
16	^{99m}Tc	Siemens LEUHR	16	8	Included
17	^{99m}Tc	Siemens LEUHR	32	8	No
18	^{99m}Tc	Siemens LEUHR	32	8	Included
19	^{99m}Tc	GE LEHR	8	8	No
20	^{99m}Tc	GE LEHR	8	8	Included
21	^{99m}Tc	GE LEHR	16	8	No
22	^{99m}Tc	GE LEHR	16	8	Included
23	^{99m}Tc	GE LEHR	32	8	No
24	^{99m}Tc	GE LEHR	32	8	Included
25	^{99m}Tc	GE LEGP	8	8	No
26	^{99m}Tc	GE LEGP	8	8	Included
27	^{99m}Tc	GE LEGP	16	8	No
28	^{99m}Tc	GE LEGP	16	8	Included
29	^{99m}Tc	GE LEGP	32	8	No
30	^{99m}Tc	GE LEGP	32	8	Included

3.6 Data Reconstruction

Normally, Simind simulates SPECT camera and forms projection images only. Reconstruct the projection images with the reconstruction programs could cause certain file type problems. In order to avoid these type of problems, smc2castor conversion program was added to Simind in 2017 [46]. Smc2castor works as Castor Reconstruction Software. In this study, this conversion program was used.

Smc2castor program has specific switches such as the number of iterations, number of subsets, activity in the phantom, time per projection, and attenuation correction. It uses MLEM optimizer, but subset number could be determined. Thus it acts like an OSEM Reconstruction Algorithm. The example of the program could be seen in Figure 3.2.



```

C:\simind>smc2castor lehrtcpoisson.h00 lehrtcpoisson/run/atten/IT:8/MB:413/TI:33

C:\simind>castor-recon -vb 1 -df lehrtcpoisson.cdh -fout lehrtcpoisson -atn lehr
tc.hct -it 8:8 -oit 8:8 -dim 128,128,128 -vox 3.00,3.00,3.00 -conf C:\Castor\con
fig -opti MLEM -proj classicSidon -flip-out Y

sOutputManager::InitOutputDirectory() -> Output path is 'lehrtcpoisson'
oProjectorManager::Initialize() -> Initialize projectors and projection lines
oOptimizerManager::Initialize() -> Initialize optimizer and penalty
iOptimizerMLEM::Initialize() -> Use the MLEM optimizer
oIterativeAlgorithm::IterateCPU() -> Start algorithm for 8 iterations
oIterativeAlgorithm::IterateCPU() -> Start iteration 1/8 subset 1/8
oIterativeAlgorithm::IterateCPU() -> Start iteration 1/8 subset 2/8
oIterativeAlgorithm::IterateCPU() -> Start iteration 1/8 subset 3/8
oIterativeAlgorithm::IterateCPU() -> Start iteration 1/8 subset 4/8
oIterativeAlgorithm::IterateCPU() -> Start iteration 1/8 subset 5/8

```

Figure 3.2 A screenshot : smc2castor program is working.

3.7 Statistical Calculations and Analysis

The tumor has a fixed location in the phantom and in order to study especially small adenoma, the volume of interest was chosen to contain all compartments of 3x3x3 pixels. The size of the adenoma is 0.58 cm³. For the region of interest, 9 pixels in one

slice was selected for statistical calculations after the reconstruction process. On the other hand, 512 pixels were chosen for the background region of interest. The large area was chosen for background calculations because this gives more accurate results. The mean pixel value and the standard deviation were calculated for the adenoma and background region of interest. Contrast and CNR (contrast to noise ratio) were calculated for each collimator and iteration case.

The difference between the image densities of two areas is identified the measurement of the contrast. In nuclear medicine studies, a high ratio between lesion and background is wanted because this increases contrast. Therefore the type of radiotracer is significant for contrast. In the Eq. 3.1, μ_a is the mean value of the counting rate of the adenoma and μ_b is the mean value of the counting rate of the background region of interest.

$$C = \frac{\mu_a - \mu_b}{\mu_b} \quad (3.1)$$

The second parameter that is used for statistical calculations is noise. Noise could be systematic or random. Systematic noise could come from measuring instrument artifacts, it refers to non-random variations in counting rates [9]. On the other hand, random noise is unpredictable and the changes in count rates are irregular. Random errors generally have a Gaussian normal distribution.

CNR is the critical parameter for lesion detectability. In literature, CNR calculation does not have a standard. In certain SPECT studies, calculated CNR were given below.

According to Dependence of left ventricular functional parameters on image acquisition time in cardiac-gated myocardial perfusion SPECT(2015) [49] and Optimization of image acquisition and reconstruction of ¹¹¹In-pentetreotide SPECT(2012)

[8] studies, CNR was calculated as the Eq. 3.2, where $\mu_M - \mu_B$ is the difference between the mean voxel value on the related ROI and mean voxel value on the background ROI, and σ_B is the standard deviation of voxels on the background ROI [49].

$$CNR = \frac{\mu_M - \mu_B}{\sigma_B} \quad (3.2)$$

Eq. 3.2 was also used in the Quantitative comparison of 124I PET/CT and 131I SPECT/CT detectability (2016) study [50].

In a Comparative analysis of cadmium-zinc-telluride cameras dedicated to myocardial perfusion SPECT (2016) study [51], related ROI's standard deviation was added in noise calculation as Eq. 3.3.

$$CNR = \frac{\mu_M - \mu_B}{\sqrt{\sigma_M^2 + \sigma_B^2}} \quad (3.3)$$

where, σ_M is the standard deviation of voxels on the interested ROI. In Ultra high-resolution SPECT for small animal imaging: Monte Carlo simulation (2011) study [52], CNR was calculated as Eq. 3.3.

One other CNR calculation in Hybrid SPECT/cardiac-gated first-pass perfusion CT: locating transplanted cells relative to infarcted myocardial targets(2012) study [53] as follows,

$$CNR = \frac{Signal - Background}{SD(background)} \quad (3.4)$$

where Signal is sum of the counts in the related VOI, the background is the mean of the sum of the counts in each background voxels VOIs, and SD of background is the standard deviation of the sum of the counts each voxel of the background VOIs [53].

In this study, mean voxel values of adenoma and background and standard deviation of the background mean were used for CNR calculation as Eq. 3.5.

$$CNR = \frac{\mu_M - \mu_B}{\sigma_{\mu_B}} \quad (3.5)$$

where μ_M is the mean voxel value of the adenoma, μ_B is the mean voxel value of the background, and σ_{μ_B} is the standard deviation of the mean voxel value of the background.

4. RESULTS

4.1 Output File Examples of the SIMIND Phantom Simulation

4.1.1 Siemens Symbia Gamma Camera Phantom Simulation Output File for LEUHR Collimator

```

SIMIND Monte Carlo Simulation Program      V6.1
-----
InputFile: tech          Collimator:pb_sb      SourceFile:smap
OutputFile:leuhrtcsc    Cover:      al          SourceMap: vox_man
Phantom(S):h2o          Crystal:   nai          DensityMap:vox_man
Phantom(B):bone        BackScatt: pmt          ScoreFile: scattwin
-----

PhotonEnergy            140.00  tc99m    PhotonsPerProj        29884340
SourceType              ZubalVoxman  sy-leuh  Activity              13631.000
PhantomType            ZubalVoxman  SPECT    DetectorLenght        29.550
DetectorWidth          22.000    BScatt   DetectorHeight        0.950
UpperEneWindowTresh    147.000  Random   Distance to det       31.000
LowerEneWindowTresh    133.000  Cover    ShiftSource (X)       0.000
PixelSize (I)          0.300    Phantom  ShiftSource (Y)       0.000
PixelSize (J)          0.300    Resolut  ShiftSource (Z)       0.000
HalfLength (S)         30.000    SaveMAP  HalfLength (P)        30.000
HalfWidth (S)          0.000                    HalfWidth (P)         0.000
HalfHeight (S)         0.000                    HalfHeigh (P)         0.000
EnergyResolution       9.900                    MaxScatterOrder       3
-----

GENERAL DATA

keV/channel            1.000                    Compiler              INTEL Windows
Photons/Bq             0.898                    StartingAngle         0.000
CameraOffset (X)      0.000                    CoverThickness        0.100

```

CameraOffset (Y)	0.000	BackscatterThickn	5.000
MatrixSize (I)	128	IntrinsicResolut	0.300
MatrixSize (J)	128	AcceptanceAngle	1.985
Emission type	2.000	Initial Weight	0.40970E+03
"NN" Scaling factor	1.000	Energy Channels	512
Photon Exit phantom	1	CutoffEnergy	0.000

Random number generator: ranMar

SPECT DATA

RotationMode	180.000	Nr of projection	48
RotationAngle	3.750	Projection start	1
Orbital fraction	1.000	Projection end	48

COLLIMATOR DATA FOR ROUTINE:Ray-Tracing by MC

CollimatorCode	sy-leuh	CollimatorType	Parallel
HoleSize (X)	0.116	Distance (X)	0.013
HoleSize (Y)	0.134	Distance (Y)	0.078
CenterShift (X)	0.065	Collimator effic	0.017
CenterShift (Y)	0.112	CollimThickness	3.580
Hole Shape	Hexagonal	Space Coll2Det	0.000
X-Ray flag	0		
CollDepValue (57)	0.000	CollDepValue(58)	0.000
CollDepValue (59)	0.000	CollDepValue(60)	0.000

NON-HOMOGENEOUS PHANTOM DATA

RotationCentre	65, 65	Bone definition	1.190
CT-Pixel size	0.240	Slice thickness	0.247
StartImage	1	No of CT-Images	243
StepSize	0.500	CTmapOrientation	0
MatrixSize (I)	128	MatrixSize (J)	128
CenterPoint (I)	65.000	CenterPoint (J)	65.000
CenterPoint (K)	122.500	ShiftPhantom (X)	0.000
ShiftPhantom (Y)	0.000	ShiftPhantom (Z)	0.000

PHANTOM DATA FROM FILE: vox_man.zub SECTION: 1

ORGAN	DENSITY	PIXELS	VOLUME(CC)	MBQ	MBQ/CC	VALUE
skin	1.090	293757	0.418E+04	0.402E+04	0.962E+00	30.0
brain	1.040	18196	0.259E+03	0.249E+03	0.962E+00	30.0
spinal cord	1.038	3589	0.510E+02	0.491E+02	0.962E+00	30.0
skull	1.610	8550	0.122E+03	0.117E+03	0.962E+00	30.0
spine	1.330	16517	0.235E+03	0.226E+03	0.962E+00	30.0
rib cage\& ster	1.410	31674	0.450E+03	0.433E+03	0.962E+00	30.0
pelvis	1.290	14419	0.205E+03	0.197E+03	0.962E+00	30.0
long bones	1.330	9771	0.139E+03	0.134E+03	0.962E+00	30.0
skeletal muscle	1.050	361640	0.514E+04	0.495E+04	0.962E+00	30.0
lungs	0.260	62374	0.887E+03	0.854E+03	0.962E+00	30.0
heart	1.060	9354	0.133E+03	0.128E+03	0.962E+00	30.0
liver	1.060	30192	0.429E+03	0.413E+03	0.962E+00	30.0
gall bladder	1.026	329	0.468E+01	0.450E+01	0.962E+00	30.0
kidney	1.050	7618	0.108E+03	0.104E+03	0.962E+00	30.0
pharynx	1.000	264	0.375E+01	0.361E+01	0.962E+00	30.0
esophagus	1.030	642	0.913E+01	0.878E+01	0.962E+00	30.0
stomach	1.030	5133	0.730E+02	0.702E+02	0.962E+00	30.0
small bowel	1.030	26447	0.376E+03	0.362E+03	0.962E+00	30.0
colon	1.030	18284	0.260E+03	0.250E+03	0.962E+00	30.0
pancreas	1.040	792	0.113E+02	0.108E+02	0.962E+00	30.0
adrenals	1.025	62	0.882E+00	0.848E+00	0.962E+00	30.0
fat	0.950	568	0.808E+01	0.777E+01	0.962E+00	30.0
blood pool	1.060	17290	0.246E+03	0.237E+03	0.962E+00	30.0
gas (bowel)	0.260	3167	0.450E+02	0.433E+02	0.962E+00	30.0
fluid (bowel)	1.007	528	0.751E+01	0.723E+01	0.962E+00	30.0
bone marrow	1.030	21170	0.301E+03	0.290E+03	0.962E+00	30.0
lymph nodes	1.030	0	0.000E+00	0.000E+00	0.000E+00	30.0
thyroid	1.050	105	0.149E+01	0.144E+01	0.962E+00	30.0
trachea	1.000	902	0.128E+02	0.123E+02	0.962E+00	30.0
cartilage	1.100	1124	0.160E+02	0.154E+02	0.962E+00	30.0
spleen	1.060	5568	0.792E+02	0.762E+02	0.962E+00	30.0
urine	1.030	6597	0.938E+02	0.903E+02	0.962E+00	30.0

feces	1.010	1134	0.161E+02	0.155E+02	0.962E+00	30.0
testes	1.040	1731	0.246E+02	0.237E+02	0.962E+00	30.0
prostate	1.045	438	0.623E+01	0.599E+01	0.962E+00	30.0
rectum	1.030	1467	0.209E+02	0.201E+02	0.962E+00	30.0
diaphragm	1.030	4528	0.644E+02	0.620E+02	0.962E+00	30.0
bladder	1.040	3147	0.448E+02	0.431E+02	0.962E+00	30.0
lesion	1.060	0	0.000E+00	0.000E+00	0.000E+00	30.0
dens of axis	1.180	15	0.213E+00	0.205E+00	0.962E+00	30.0
jaw bone	1.680	1086	0.154E+02	0.149E+02	0.962E+00	30.0
lacrimal glands	1.045	28	0.398E+00	0.383E+00	0.962E+00	30.0
spinal canal	1.038	102	0.145E+01	0.140E+01	0.962E+00	30.0
hard palate	1.680	193	0.274E+01	0.264E+01	0.962E+00	30.0
cerebellum	1.040	2402	0.342E+02	0.329E+02	0.962E+00	30.0
tongue	1.000	588	0.836E+01	0.805E+01	0.962E+00	30.0
medulla oblongo	1.420	19	0.270E+00	0.260E+00	0.962E+00	30.0
pons	1.000	326	0.464E+01	0.446E+01	0.962E+00	30.0
uncus(ear bones	1.180	30	0.427E+00	0.411E+00	0.962E+00	30.0
sinuses	1.000	1357	0.193E+02	0.186E+02	0.962E+00	30.0
optic nerve	1.070	70	0.996E+00	0.958E+00	0.962E+00	30.0
cerebral falx	1.040	205	0.292E+01	0.281E+01	0.962E+00	30.0
eye	1.070	241	0.343E+01	0.330E+01	0.962E+00	30.0
lens	1.070	23	0.327E+00	0.315E+00	0.962E+00	30.0
cerebral aquadu	1.040	0	0.000E+00	0.000E+00	0.000E+00	30.0
teeth	1.920	268	0.381E+01	0.367E+01	0.962E+00	30.0

TUMORS ADDED FROM FILE:tech.inp

TUMOR	VOL(cc)	MBq	MBq/cc	CHANGE g/cm3
1	0.588E+00	0.999E+01	0.170E+02	none

Photon energy	Abundance
20.669keV	0.112E-01
21.023keV	0.177E-02
89.600keV	0.104E-04
140.511keV	0.885E+00
142.683keV	0.230E-03

232.700keV 0.840E-07
 322.400keV 0.960E-06

 SCATTWIN RESULTS USING WINDOW FILE: tech.win

Win	WinAdded	Range(keV)	ScaleFactor
1	0	133.0 - 147.0	1.00
2	0	147.0 - 168.0	0.33
3	0	112.0 - 133.0	0.33

Win	Total	Scatter	Primary	S/P-Ratio	S/T Ratio	Cps/MBq
1	0.831E+07	0.131E+07	0.700E+07	0.188E+00	0.158E+00	0.127E+02
2	0.132E+07	0.761E+05	0.125E+07	0.610E-01	0.575E-01	0.202E+01
3	0.590E+07	0.359E+07	0.231E+07	0.155E+01	0.608E+00	0.901E+01

Win	Geo(Air)	Pen(Air)	Sca(Air)	Geo(Tot)	Pen(Tot)	Sca(Tot)
1	95.55%	3.14%	1.31%	95.61%	3.09%	1.29%
2	95.62%	3.14%	1.24%	95.62%	3.13%	1.24%
3	95.28%	3.13%	1.59%	96.08%	2.61%	1.31%

Win	SC 1	SC 2	SC 3
1	90.8%	8.5%	0.7%
2	95.7%	4.1%	0.2%
3	72.3%	23.0%	4.6%

 Simulation start: 2018:05:06 13:30:31
 Simulation stop : 2018:05:06 19:48:16
 Elapsed time 6h 17min and 45sec

INTERACTIONS IN THE CRYSTAL

Detector hits.....:	23642324
Detector hits/sec...:	1045.
Max val in spectra..:	0.8945E+06
Max val in images...:	0.3502E+02

Count rate [Total] .: 0.6219E+06
 Count rate [Window]: 0.2367E+06

 PHOTONS AFTER 1) COLLIMATOR AND 2) WITHIN E-WIN

Geometric.....: 96.07% 95.62%
 Penetration...: 2.52% 3.09%
 Scatter Collim: 1.41% 1.29%
 X-ray Collim...: 0.00% 0.00%

 RESULTS FROM ENERGY SPECTRUM

Compton area in spectrum: 0.1668E+08 8.25% (1SD)
 Photo area in spectrum: 0.1136E+08 9.37% (1SD)
 Pileup area in spectrum: 0.1806E+07 10.40% (1SD)

 SCATTER RESULTS IN ENERGY WINDOW

Scatter/Primary.....: 0.1826E+00 5.86% (1SD)
 Scatter/Total.....: 0.1544E+00
 ScatterOrder 1: 90.9765 %
 ScatterOrder 2: 8.3479 %
 ScatterOrder 3: 0.6756 %

 CALCULATED DETECTOR PARAMETERS

Efficiency [Peak]....: 0.3629 9.37% (1SD)
 Efficiency [Detector]: 0.9534
 Sensitivity [cps/MBq]: 17.3654
 Sensitivity [cpm/uCi]: 38.5511
 Peak/Compton [Peak]..: 61.9671
 Peak/Compton [Area]..: 0.6810
 Peak/Total.....: 0.3806
 Inifile: simind.ini

 Command: tech leuhrtcsc/fz:vox_man/fi:tc99m/cc:sy-leuh/84:1/FW:tech/
 in:x22,5x/IF:tech

The energy spectra of the simulation could be seen in figure 4.1.

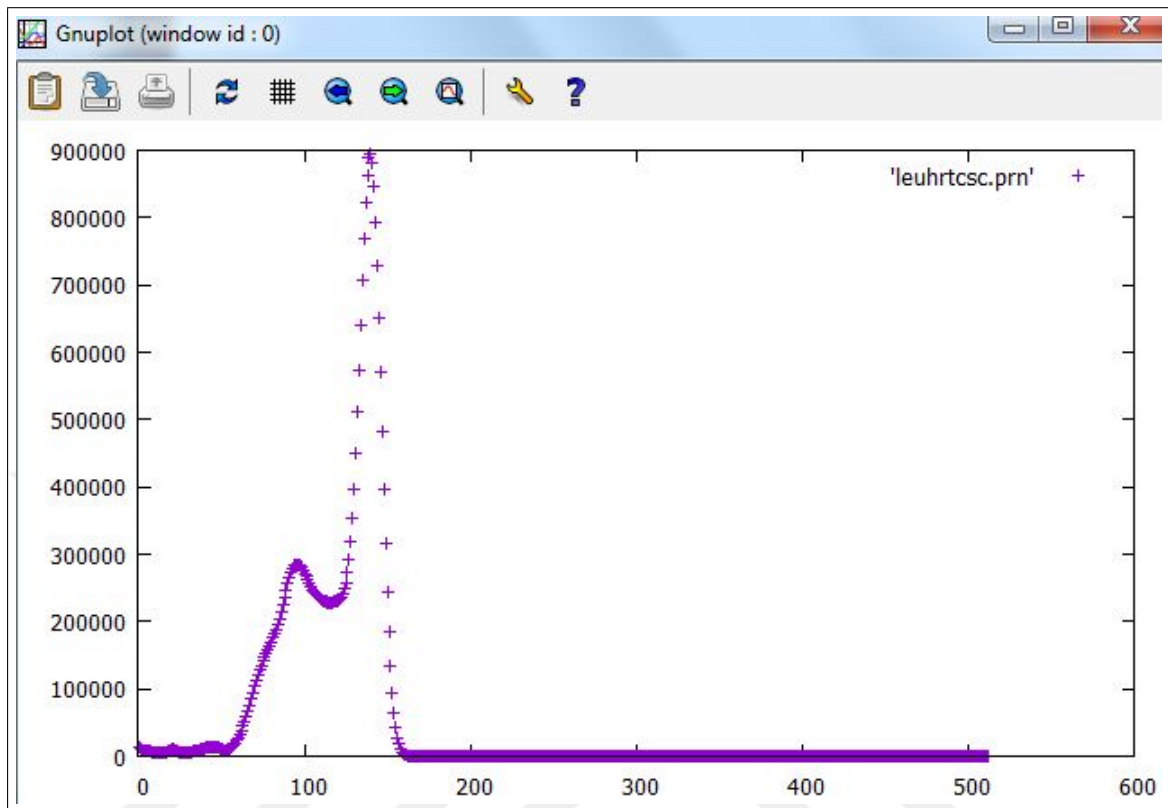


Figure 4.1 The energy Spectra of the Siemens Symbia Gamma Camera Phantom Simulation Output File for LEUHR Collimator.

4.1.2 General Electric Infinia Hawkeye Gamma Camera Phantom Simulation Output File for LEHR Collimator

SIMIND Monte Carlo Simulation Program V6.1

```
-----
InputFile: tech          Collimator:pb_sb      SourceFile:smap
OutputFile:gilehrtc     Cover:    al          SourceMap: vox_man
Phantom(S):h2o         Crystal:  nai         DensityMap:vox_man
Phantom(B):bone       BackScatt: pmt       ScoreFile: none
-----
```

```
PhotonEnergy          140.00 tc99m      PhotonsPerProj      29884340
```

SourceType	ZubalVoxman	Spectra	Activity	13631.000
PhantomType	ZubalVoxman	gi-lehr	DetectorLenght	27.000
DetectorWidth	20.000	SPECT	DetectorHeight	0.950
UpperEneWindowTresh	147.000	BScatt	Distance to det	31.000
LowerEneWindowTresh	133.000	Random	ShiftSource (X)	0.000
PixelSize (I)	0.300	Cover	ShiftSource (Y)	0.000
PixelSize (J)	0.300	Phantom	ShiftSource (Z)	0.000
HalfLength (S)	30.000	Resolut	HalfLength (P)	30.000
HalfWidth (S)	0.000	IntFile	HalfWidth (P)	0.000
HalfHeight (S)	0.000	SaveMAP	HalfHeigh (P)	0.000
EnergyResolution	9.900		MaxScatterOrder	3

GENERAL DATA

keV/channel	1.000	Compiler	INTEL Windows
Photons/Bq	0.898	StartingAngle	0.000
CameraOffset (X)	0.000	CoverThickness	0.100
CameraOffset (Y)	0.000	BackscatterThickn	5.000
MatrixSize (I)	128	IntrinsicResolut	0.300
MatrixSize (J)	128	AcceptanceAngle	2.454
Emission type	2.000	Initial Weight	0.40970E+03
"NN" Scaling factor	1.000	Energy Channels	512
Photon Exit phantom	1	CutoffEnergy	0.000

Random number generator: ranMar

SPECT DATA

RotationMode	180.000	Nr of projection	48
RotationAngle	3.750	Projection start	1
Orbital fraction	1.000	Projection end	48

COLLIMATOR DATA FOR ROUTINE:Ray-Tracing by MC

CollimatorCode	gi-lehr	CollimatorType	Parallel
HoleSize (X)	0.150	Distance (X)	0.020
HoleSize (Y)	0.173	Distance (Y)	0.104

CenterShift (X)	0.085	Collimator effic	0.021
CenterShift (Y)	0.147	CollimThickness	3.500
Hole Shape	Hexagonal	Space Coll2Det	0.000
X-Ray flag	0		
CollDepValue (57)	0.000	CollDepValue(58)	0.000
CollDepValue (59)	0.000	CollDepValue(60)	0.000

NON-HOMOGENEOUS PHANTOM DATA

RotationCentre	65, 65	Bone definition	1.190
CT-Pixel size	0.240	Slice thickness	0.247
StartImage	1	No of CT-Images	243
StepSize	0.500	CTmapOrientation	0
MatrixSize (I)	128	MatrixSize (J)	128
CenterPoint (I)	65.000	CenterPoint (J)	65.000
CenterPoint (K)	122.500	ShiftPhantom (X)	0.000
ShiftPhantom (Y)	0.000	ShiftPhantom (Z)	0.000

PHANTOM DATA FROM FILE: vox_man.zub SECTION: 1

ORGAN	DENSITY	PIXELS	VOLUME(CC)	MBQ	MBQ/CC	VALUE
skin	1.090	293757	0.418E+04	0.402E+04	0.962E+00	30.0
brain	1.040	18196	0.259E+03	0.249E+03	0.962E+00	30.0
spinal cord	1.038	3589	0.510E+02	0.491E+02	0.962E+00	30.0
skull	1.610	8550	0.122E+03	0.117E+03	0.962E+00	30.0
spine	1.330	16517	0.235E+03	0.226E+03	0.962E+00	30.0
rib cage & ster	1.410	31674	0.450E+03	0.433E+03	0.962E+00	30.0
pelvis	1.290	14419	0.205E+03	0.197E+03	0.962E+00	30.0
long bones	1.330	9771	0.139E+03	0.134E+03	0.962E+00	30.0
skeletal muscle	1.050	361640	0.514E+04	0.495E+04	0.962E+00	30.0
lungs	0.260	62374	0.887E+03	0.854E+03	0.962E+00	30.0
heart	1.060	9354	0.133E+03	0.128E+03	0.962E+00	30.0
liver	1.060	30192	0.429E+03	0.413E+03	0.962E+00	30.0
gall bladder	1.026	329	0.468E+01	0.450E+01	0.962E+00	30.0
kidney	1.050	7618	0.108E+03	0.104E+03	0.962E+00	30.0

pharynx	1.000	264	0.375E+01	0.361E+01	0.962E+00	30.0
esophagus	1.030	642	0.913E+01	0.878E+01	0.962E+00	30.0
stomach	1.030	5133	0.730E+02	0.702E+02	0.962E+00	30.0
small bowel	1.030	26447	0.376E+03	0.362E+03	0.962E+00	30.0
colon	1.030	18284	0.260E+03	0.250E+03	0.962E+00	30.0
pancreas	1.040	792	0.113E+02	0.108E+02	0.962E+00	30.0
adrenals	1.025	62	0.882E+00	0.848E+00	0.962E+00	30.0
fat	0.950	568	0.808E+01	0.777E+01	0.962E+00	30.0
blood pool	1.060	17290	0.246E+03	0.237E+03	0.962E+00	30.0
gas (bowel)	0.260	3167	0.450E+02	0.433E+02	0.962E+00	30.0
fluid (bowel)	1.007	528	0.751E+01	0.723E+01	0.962E+00	30.0
bone marrow	1.030	21170	0.301E+03	0.290E+03	0.962E+00	30.0
lymph nodes	1.030	0	0.000E+00	0.000E+00	0.000E+00	30.0
thyroid	1.050	105	0.149E+01	0.144E+01	0.962E+00	30.0
trachea	1.000	902	0.128E+02	0.123E+02	0.962E+00	30.0
cartilage	1.100	1124	0.160E+02	0.154E+02	0.962E+00	30.0
spleen	1.060	5568	0.792E+02	0.762E+02	0.962E+00	30.0
urine	1.030	6597	0.938E+02	0.903E+02	0.962E+00	30.0
feces	1.010	1134	0.161E+02	0.155E+02	0.962E+00	30.0
testes	1.040	1731	0.246E+02	0.237E+02	0.962E+00	30.0
prostate	1.045	438	0.623E+01	0.599E+01	0.962E+00	30.0
rectum	1.030	1467	0.209E+02	0.201E+02	0.962E+00	30.0
diaphragm	1.030	4528	0.644E+02	0.620E+02	0.962E+00	30.0
bladder	1.040	3147	0.448E+02	0.431E+02	0.962E+00	30.0
lesion	1.060	0	0.000E+00	0.000E+00	0.000E+00	30.0
dens of axis	1.180	15	0.213E+00	0.205E+00	0.962E+00	30.0
jaw bone	1.680	1086	0.154E+02	0.149E+02	0.962E+00	30.0
lacrimal glands	1.045	28	0.398E+00	0.383E+00	0.962E+00	30.0
spinal canal	1.038	102	0.145E+01	0.140E+01	0.962E+00	30.0
hard palate	1.680	193	0.274E+01	0.264E+01	0.962E+00	30.0
cerebellum	1.040	2402	0.342E+02	0.329E+02	0.962E+00	30.0
tongue	1.000	588	0.836E+01	0.805E+01	0.962E+00	30.0
medulla oblongo	1.420	19	0.270E+00	0.260E+00	0.962E+00	30.0
pons	1.000	326	0.464E+01	0.446E+01	0.962E+00	30.0

uncus(ear bones	1.180	30	0.427E+00	0.411E+00	0.962E+00	30.0
sinuses	1.000	1357	0.193E+02	0.186E+02	0.962E+00	30.0
optic nerve	1.070	70	0.996E+00	0.958E+00	0.962E+00	30.0
cerebral falx	1.040	205	0.292E+01	0.281E+01	0.962E+00	30.0
eye	1.070	241	0.343E+01	0.330E+01	0.962E+00	30.0
lens	1.070	23	0.327E+00	0.315E+00	0.962E+00	30.0
cerebral aquadu	1.040	0	0.000E+00	0.000E+00	0.000E+00	30.0
teeth	1.920	268	0.381E+01	0.367E+01	0.962E+00	30.0

TUMORS ADDED FROM FILE:tech.inp

TUMOR	VOL(cc)	MBq	MBq/cc	CHANGE g/cm3
1	0.588E+00	0.999E+01	0.170E+02	none

Photon energy	Abundance
20.669keV	0.112E-01
21.023keV	0.177E-02
89.600keV	0.104E-04
140.511keV	0.885E+00
142.683keV	0.230E-03
232.700keV	0.840E-07
322.400keV	0.960E-06

Simulation start: 2018:05:06 19:48:16

Simulation stop : 2018:05:07 01:52:54

Elapsed time 6h 4min and 38sec

Header file gilehrtc.h00

Image file gilehrtc.a00

INTERACTIONS IN THE CRYSTAL

Detector hits.....:	24310116
Detector hits/sec...:	1113.
Max val in spectra.:	0.1479E+07
Max val in images..:	0.5320E+02
Count rate [Total].:	0.1041E+07
Count rate [Window]:	0.3958E+06

PHOTONS AFTER 1) COLLIMATOR AND 2) WITHIN E-WIN

Geometric.....: 96.31% 95.91%
Penetration...: 2.42% 2.97%
Scatter Collim: 1.27% 1.12%
X-ray Collim..: 0.00% 0.00%

RESULTS FROM ENERGY SPECTRUM

Compton area in spectrum: 0.2793E+08 8.40% (1SD)
Photo area in spectrum: 0.1900E+08 9.43% (1SD)
Pileup area in spectrum: 0.3020E+07 10.46% (1SD)

SCATTER RESULTS IN ENERGY WINDOW

Scatter/Primary.....: 0.1829E+00 6.07% (1SD)
Scatter/Total.....: 0.1546E+00
ScatterOrder 1: 90.9669 %
ScatterOrder 2: 8.3581 %
ScatterOrder 3: 0.6751 %

CALCULATED DETECTOR PARAMETERS

Efficiency [Peak]....: 0.3626 9.43% (1SD)
Efficiency [Detector]: 0.9533
Sensitivity [cps/MBq]: 29.0376
Sensitivity [cpm/uCi]: 64.4635
Peak/Compton [Peak]..: 61.0591
Peak/Compton [Area]..: 0.6803
Peak/Total.....: 0.3804
Inifile: simind.ini

Command: tech GIllehrtc/fz:vox_man/fi:tc99m/cc:gi-lehr/in:x22,5x/IF:tech

The energy spectra of the simulation could be seen in figure 4.2.

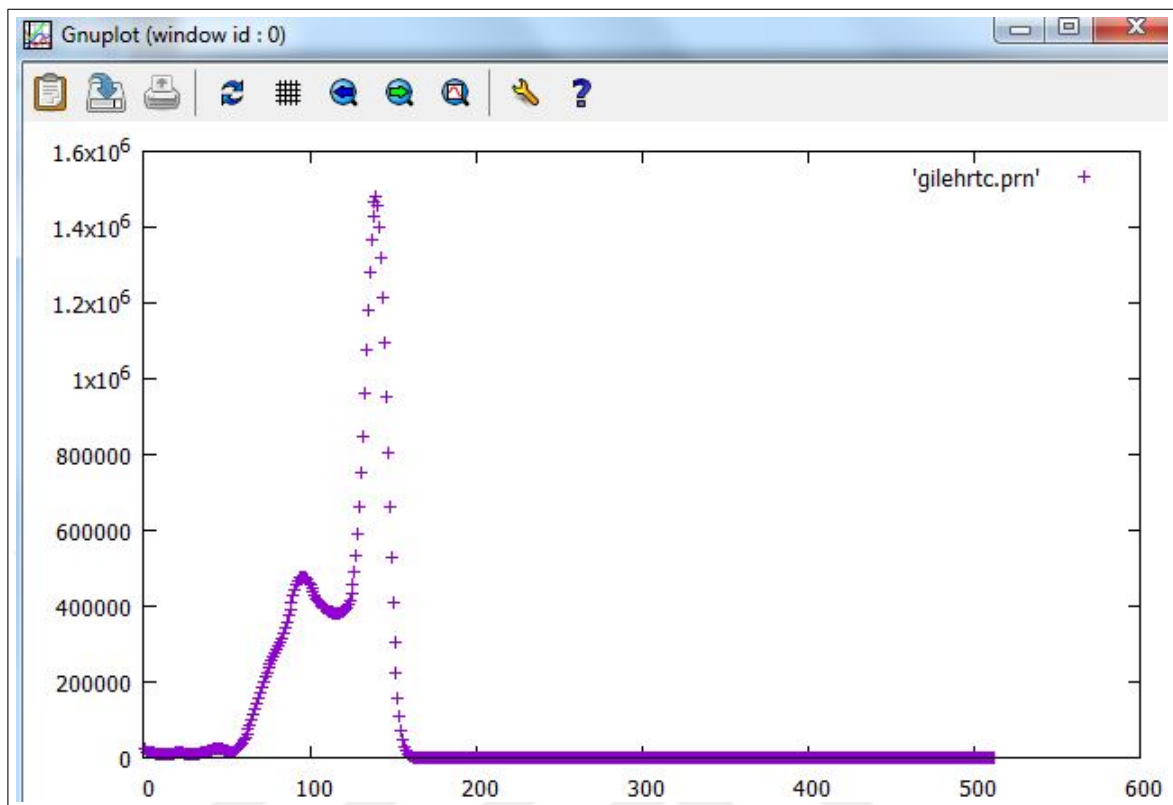


Figure 4.2 The energy Spectra of the GE Infinia Hawkeye Gamma Camera Phantom Simulation Output File for LEHR Collimator.

4.2 Reconstructed Images and Calculations

4.2.1 Results without Poisson Noise

4.2.1.1 Siemens Symbia Gamma Camera.

Siemens LEHR, MELP and LEUHR collimator types were used. For all cases, attenuation corrections were included. Contrast values could be seen in Table 4.1, Table 4.2 and Table 4.3. Number of counts were found consistent in the literature [54].

Table 4.1

Adenoma and background counts and contrast values for different parameters in Siemens LEHR collimator when Poisson Noise was not included.

ID	Collimator	IT No	SC CR	Adenoma	Background	Contrast
1	sy-lehr	8	-	418	338	0.24
2	sy-lehr	8	+	352	279	0.26
3	sy-lehr	16	-	448	339	0.32
4	sy-lehr	16	+	382	278	0.37
5	sy-lehr	32	-	469	339	0.38
6	sy-lehr	32	+	404	278,8	0.45

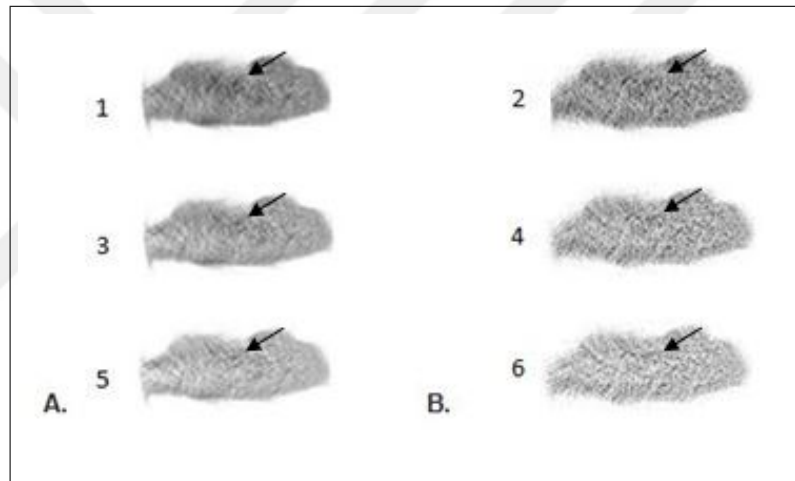


Figure 4.3 A. Transversal images for Siemens LEHR collimator without scatter correction B. Transversal images for Siemens LEHR collimator with scatter correction. Numbers on the left of the images are ID numbers.

Table 4.2

Adenoma and background counts and contrast values for different parameters in Siemens MELP collimator when Poisson Noise was not included.

ID	Collimator	IT No	SC CR	Adenoma	Background	Contrast
7	sy-melp	8	-	1320	1165.8	0.13
8	sy-melp	8	+	823	971	-0.15
9	sy-melp	16	-	1434	1168.2	0.23
10	sy-melp	16	+	817	970	-0.16
11	sy-melp	32	-	1511	1170.7	0.29
12	sy-melp	32	+	788	972	-0.19

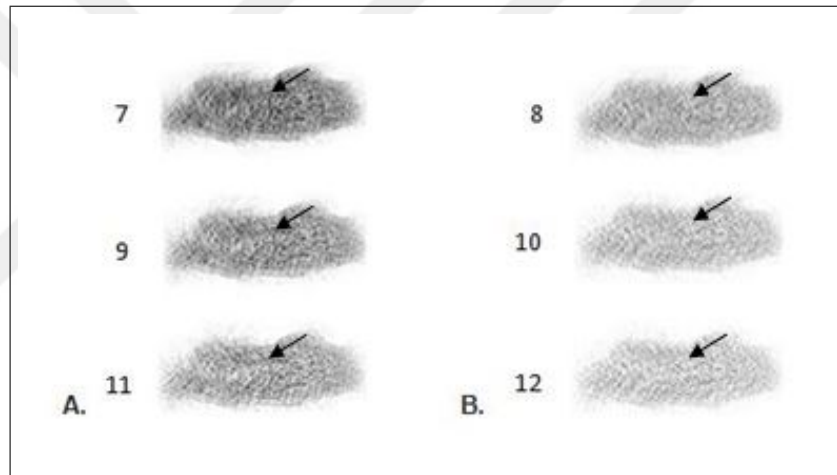


Figure 4.4 A. Transversal images for Siemens MELP collimator without scatter correction B. Transversal images for Siemens MELP collimator with scatter correction. Numbers on the left of the images are ID numbers.

Table 4.3

Adenoma and background counts and contrast values for different parameters in Siemens LEUHR collimator when Poisson Noise was not included.

ID	Collimator	IT No	SC CR	Adenoma	Background	Contrast
13	sy-leuhr	8	-	284	171	0.66
14	sy-leuhr	8	+	218	139	0.57
15	sy-leuhr	16	-	308	171,6	0.79
16	sy-leuhr	16	+	225	138	0.63
17	sy-leuhr	32	-	323	171.8	0.88
18	sy-leuhr	32	+	222	139	0.60

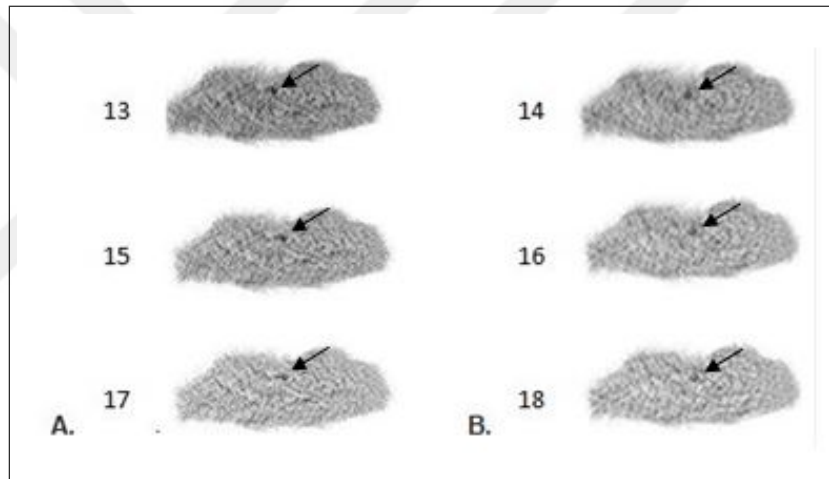


Figure 4.5 A. Transversal images for Siemens LEUHR collimator without scatter correction B. Transversal images for Siemens LEUHR collimator with scatter correction. Numbers on the left of the images are ID numbers.

4.2.1.2 General Electric Infinia Hawkeye Gamma Camera.

General Electric Infinia LEHR and LEGP collimator types were used. For all cases, attenuation corrections were included. Contrast values could be seen in Table 4.4 and Table 4.5.

Table 4.4

Adenoma and background counts and contrast values for different parameters in GE Infinia LEHR collimator when Poisson Noise was not included.

ID	Collimator	IT No	SC CR	Adenoma	Background	Contrast
19	gi-lehr	8	-	400	284,6	0.41
20	gi-lehr	8	+	299,7	236	0.27
21	gi-lehr	16	-	416,8	284,3	0.47
22	gi-lehr	16	+	311	236	0.32
23	gi-lehr	32	-	416,7	284,5	0.46
24	gi-lehr	32	+	314	236	0.33

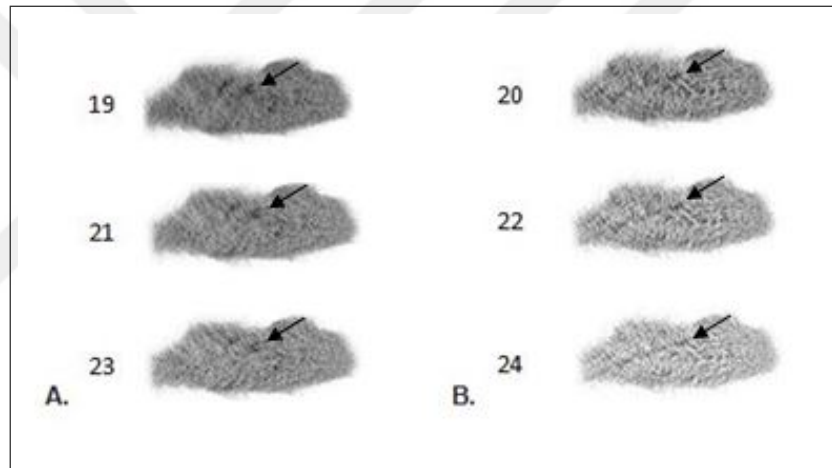


Figure 4.6 A. Transversal images for GE Infinia LEHR collimator without scatter correction B. Transversal images for GE Infinia LEHR collimator with scatter correction. Numbers on the left of the images are ID numbers.

Table 4.5

Adenoma and background counts and contrast values for different parameters in GE Infinia LEGP collimator when Poisson Noise was not included.

ID	Collimator	IT No	SC CR	Adenoma	Background	Contrast
25	gi-legp	8	-	593,4	489,7	0.21
26	gi-legp	8	+	460,7	407,2	0.13
27	gi-legp	16	-	621	489,7	0.27
28	gi-legp	16	+	475,9	406,7	0.17
29	gi-legp	32	-	622,2	488	0.28
30	gi-legp	32	+	472,8	406,5	0.16

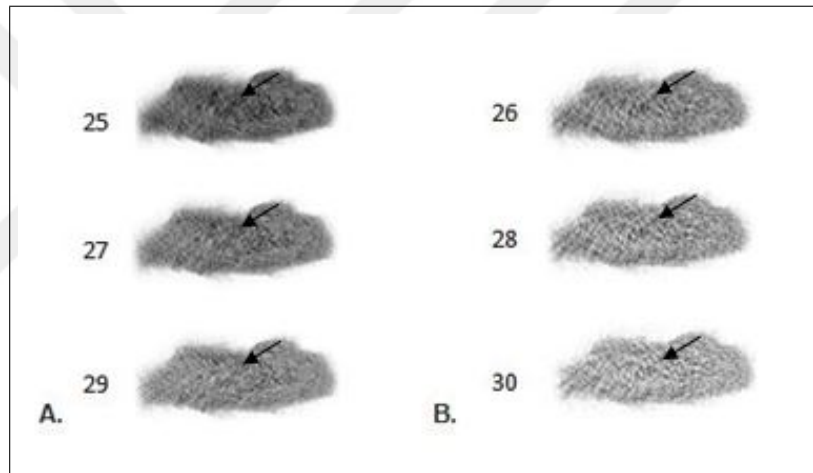


Figure 4.7 A. Transversal images for GE Infinia LEGP collimator without scatter correction B. Transversal images for GE Infinia LEGP collimator with scatter correction. Numbers on the left of the images are ID numbers.

4.3 Results with Poisson Noise

4.3.1 Poisson Noise Addition for Siemens Symbia Gamma Camera

In order to add Poisson noise to the images, Poisson noise plugin in ImageJ was used [55] and the cases were repeated. For all cases, attenuation correction was included.

Table 4.6

Adenoma and background counts and contrast values for different parameters in Siemens LEHR collimator when Poisson Noise was included.

ID	Collimator	IT NO	SC	Adenoma	BG	Contrast	SD of BGmean	CNR
1p	sy-lehr	8	-	506	340	0.49	75,67	2.19
2p	sy-lehr	8	+	468	279	0.68	66	2.86
3p	sy-lehr	16	-	569	340,3	0.67	93	2.46
4p	sy-lehr	16	+	493	280	0.76	82,67	2.58
5p	sy-lehr	32	-	599	339,7	0.76	106,67	2.43
6p	sy-lehr	32	+	517	280,3	0.84	95,43	2.48

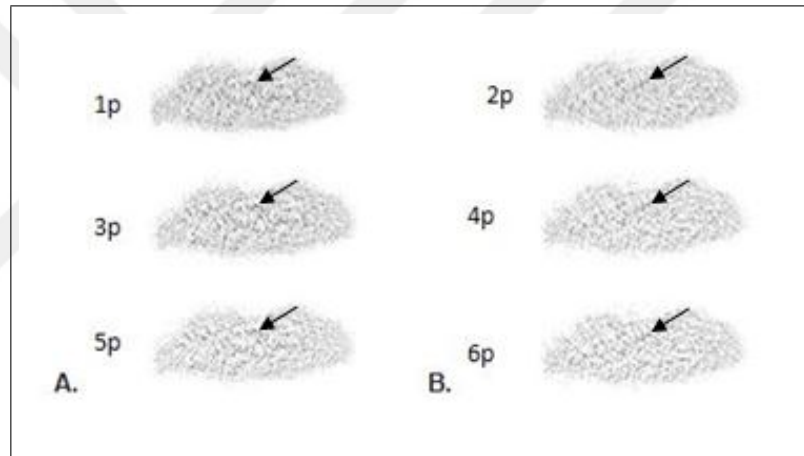


Figure 4.8 A. Transversal images for Siemens LEHR collimator without scatter correction B. Transversal images for Siemens LEHR collimator with scatter correction. Numbers on the left of the images are ID numbers. Poisson noise was included.

Table 4.7

Adenoma and background counts and contrast values for different parameters in Siemens MELP collimator when Poisson Noise was included.

ID	Collimator	IT NO	SC	Adenoma	BG	Contrast	SD of BGmean	CNR
7p	sy-melp	8	-	1072	1164	-0.08	154	-0.60
8p	sy-melp	8	+	979,3	966,6	0.01	142,33	0.09
9p	sy-melp	16	-	1180	1169	0.01	197,33	0.06
10p	sy-melp	16	+	988	965	0.02	184,67	0.12
11p	sy-melp	32	-	1263	1190	0.06	264,33	0.28
12p	sy-melp	32	+	910	965,7	-0.06	223	-0.25

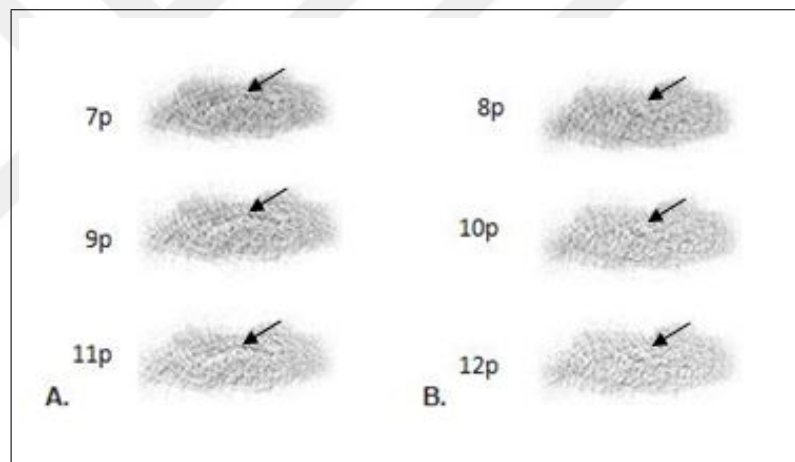


Figure 4.9 A. Transversal images for Siemens MELP collimator without scatter correction B. Transversal images for Siemens MELP collimator with scatter correction. Numbers on the left of the images are ID numbers. Poisson noise was included.

Table 4.8

Adenoma and background counts and contrast values for different parameters in Siemens LEUHR collimator when Poisson Noise was included.

ID	Collimator	IT NO	SC	Adenoma	BG	Contrast	SD of BGmean	CNR
13p	sy-leuhr	8	-	332	166	1.00	47	3.53
14p	sy-leuhr	8	+	200	139	0.44	42	1.45
15p	sy-leuhr	16	-	371,5	165,8	1.24	55	3.74
16p	sy-leuhr	16	+	210	139,4	0.51	44,3	1.59
17p	sy-leuhr	32	-	357	165,9	1.15	52	3.68
18p	sy-leuhr	32	+	223	141,8	0.57	51	1.58

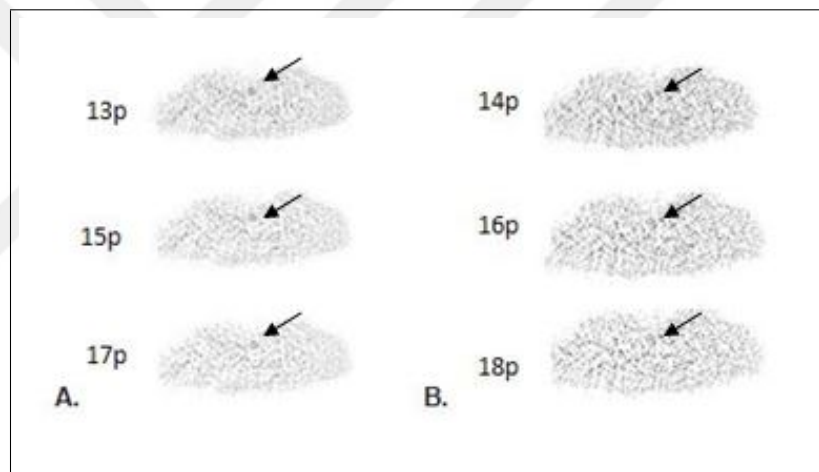


Figure 4.10 A. Transversal images for Siemens LEUHR collimator without scatter correction B. Transversal images for Siemens LEUHR collimator with scatter correction. Numbers on the left of the images are ID numbers. Poisson noise was included.

4.3.2 Poisson Noise Addition for GE Infinia Hawkeye Gamma Camera

Table 4.9

Adenoma and background counts and contrast values for different parameters in GE Infinia LEHR collimator when Poisson Noise was included.

ID	Collimator	IT NO	SC	Adenoma	BG	Contrast	SD of BGmean	CNR
19p	gi-lehr	8	-	470,6	290	0.62	66,3	2.72
20p	gi-lehr	8	+	402	243,5	0.72	59	2.69
21p	gi-lehr	16	-	514,6	289	0.78	80,3	2.81
22p	gi-lehr	16	+	414	234	0.77	67,6	2.66
23p	gi-lehr	32	-	535,9	289	0,85	90,6	2.72
24p	gi-lehr	32	+	397,2	234,2	0.70	79,6	2.05

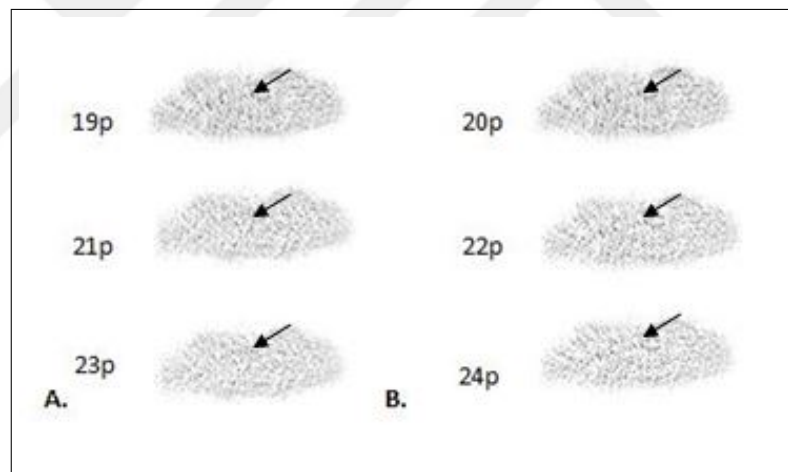


Figure 4.11 A. Transversal images for GE LEHR collimator without scatter correction B. Transversal images for GE LEHR collimator with scatter correction. Numbers on the left of the images are ID numbers. Poisson noise was included.

Table 4.10

Adenoma and background counts and contrast values for different parameters in GE Infinia LEGP collimator when Poisson Noise was included.

ID	Collimator	IT NO	SC	Adenoma	BG	Contrast	SD of BGmean	CNR
25p	gi-legp	8	-	443,2	493	0.10	95,33	0.53
26p	gi-legp	8	+	423	412	0.03	80	0.14
27p	gi-legp	16	-	519,4	493	0.05	118	0.22
28p	gi-legp	16	+	390	410	-0.05	100,6	-0.20
29p	gi-legp	32	-	452,2	493	-0.08	136,6	-0.30
30p	gi-legp	32	+	386	409	-0.06	117	-0.20

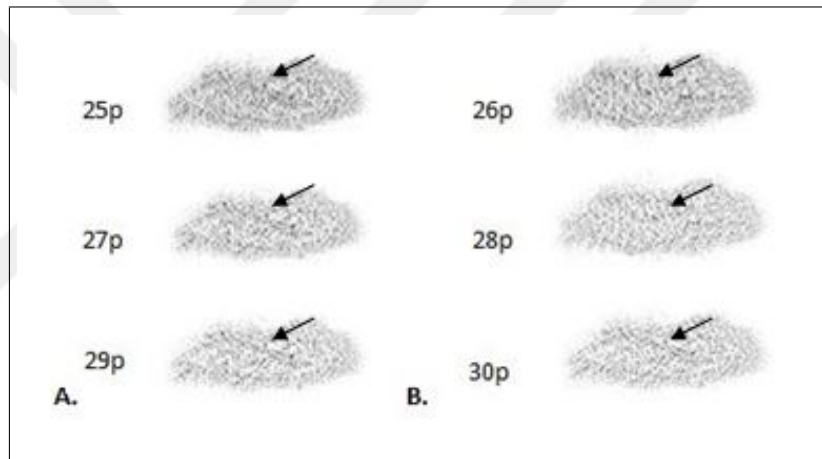


Figure 4.12 A. Transversal images for GE LEGP collimator without scatter correction B. Transversal images for GE LEGP collimator with scatter correction. Numbers on the left of the images are ID numbers. Poisson noise was included.

4.4 Summary of the Results

For Siemens Symbia Gamma Camera, adenoma could be seen in LEUHR collimators who have the best contrasts according to the results. In figure 4.13 - B, adenoma could be seen (Siemens LEHR 8,16,32 iterations) and C is the worst case, nothing could be seen (Siemens MELP 8,16,32 iterations) when there is no scatter correction and Poisson noise as Figure 4.13. These results are coherent with literature [7, 19, 34, 35]. Low energy high resolution collimators showed better CNR values. LEUHR collimator with 16 iterations showed the best result [7].

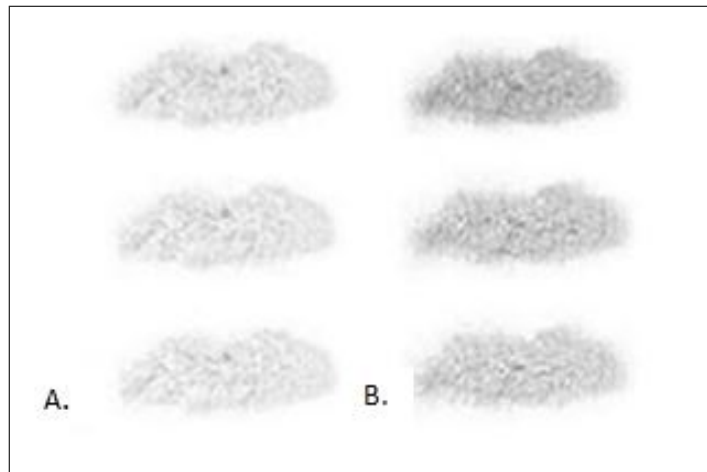


Figure 4.13 A. Transversal images for Siemens LEUHR from top to bottom 8,16 and 32 iterations without scatter correction (sc) and with poisson noise (ID:13p,15p,17p) B. Transversal images for Siemens MELP from top to bottom 8,16 and 32 iterations with sc and with poisson noise (ID:8p,10p,12p).

For General Electric Hawkeye Gamma Camera, LEHR collimator (when without scatter correction and without Poisson noise) seems better than the others as the best and the worst images could be seen in Figure 4.14.

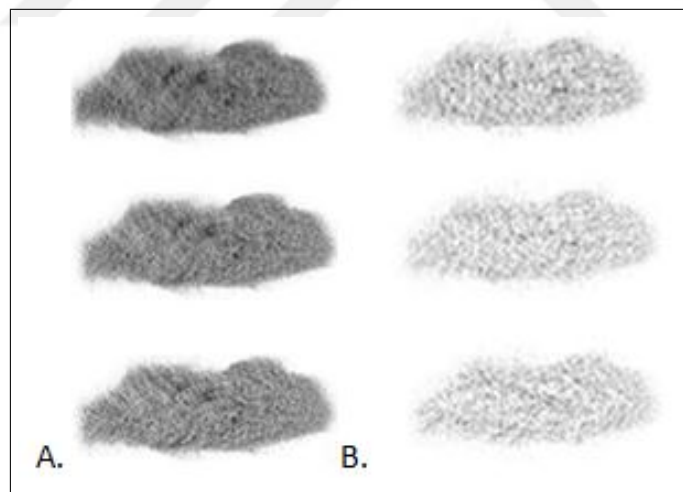


Figure 4.14 A. The best cases for GE Infinia Hawkeye Gamma Camera. Transversal images for LEHR from top to bottom 8,16 and 32 iterations without scatter correction (sc) and with poisson noise (ID:19,21,23) . B. The worst cases for GE Infinia Hawkeye Gamma Camera. Transversal images for LEGP from top to bottom 8,16 and 32 iterations with sc and with poisson noise (ID:26p,28p,30p).

In literature, two energy window settings and 6,8,16,32 iterations with Siemens gamma camera were used. According to these parameters, mean contrast values in literature [7] could be seen in fig 4.15.

Collimator, Energy Window, Correction	Contrast _{mean}
MELP, Clinical, SC+	2 %
MELP, Clinical, SC-	9 %
MELP, Test, SC-	25 %
MELP, Test, SC+	37 %
LEHR, Clinical, SC-	9 %
LEHR, Clinical, SC+	9 %
LEHR, Test, SC-	30%
LEHR, Test, SC+	55 %
LEUHR, Clinical, SC-	30 %
LEUHR, Clinical, SC+	50 %
LEUHR, Test, SC-	67 %
LEUHR, Test, SC+	4 %

Collimator, Correction	Mean Contrast
MELP, SC-	0
MELP, SC+	0
LEHR, SC-	64%
LEHR, SC+	76%
LEUHR, SC -	113%
LEUHR, SC +	50%

Figure 4.15 Tables for comparison in literature. In first table, results shows mean contrast values and in literature. 6,8,16,32 iterations with only Siemens Symbia gamma camera were examined. In second table shows mean contrast values from this study.

5. DISCUSSION

According to the results, in certain collimators contrast and CNR increase as number of iterations increases in MLEM reconstruction algorithm (8,16,32) for both without noisy and with noisy images.

In general, scatter correction did not result in a significant improvement in this study, the reason could be the low pixel numbers for the adenoma (nine pixels). On the other hand, these low pixel number of adenoma could explain big count fluctuations between without noisy and with noisy images (when other parameters are same).

The results showed that MELP and LEGP collimators could not be convenient for parathyroid SPECT imaging because contrast and CNR values look very low.

The high-resolution collimator (LEUHR) gave the best results for contrast and CNR. The guidelines [34] recommend high-resolution collimator for image acquisition, as a consequence these results are expected. The simulation shows the same results in a literature. LEUHR collimator with 16 iterations shows better result than LEUHR with 32 iterations. The reason could be that as iteration number increases, noise increases, too [7]. This study could show that doing experiments with simulation methods, that only needs computer and software, could give reliable and close results to the real cases.

Siemens LEHR collimator and GE Infinia LEHR collimator show different contrast values. These two collimators have the same names but different properties, so they could show different results. The study indicates the simulation could be carried out with different gamma camera brands. In this way, optimal parameters for each brand could be found with this simulation method. The study has this flexibility. Through these type of simulation studies, optimal parameters for various devices for SPECT could be performed less costly. Furthermore, this could be done in a shorter time in comparison with using real SPECT device studies.

For certain images, the artifactual blobs look same to parathyroid adenoma. However,

that misinterpretation could be kept away with the contribution of CT, and the examination of the anatomical reference [7].

According to parathyroid Tc- I subtraction studies in literature, Tc and I images are acquired simultaneously after injected these two radiopharmaceuticals to the patient. This simultaneous image formation could be done through energy window differences. The primary benefit of this technique is there are no extra radiation and no patient motion artifacts in the subtraction image due to the simultaneous acquisition [35]. This work has concentrated on a single isotope (delayed imaging) protocol. According to the guidelines separate double isotope acquisitions or simultaneous double isotope studies could be done [35]. Future work may consider double isotope studies.

Future work will concentrate on the exact quantification of adenoma volume and its uptake. Furthermore, precise quantification and characterization (whether it is an adenoma or not) could be studied.

6. CONCLUSION

It was found that the optimal parameters were LEUHR collimator, 16 iterations, and no scatter correction with Poisson noise for Siemens Symbia gamma camera (CNR:3.74). LEHR collimator, 16 iterations, without scatter correction, with Poisson noise gave better result compared to the other parameters for General Electric Infinia Hawkeye gamma camera (CNR:2.81).

This study shows that a small parathyroid adenoma could be studied with computer simulation methods. The simulation with Simind could be carried out with different gamma camera brands. Doing experiments with simulation methods, that only need computer and software, could give reliable and close results to the real cases. Thus the optimal parameters could be investigated for every different machine with changing parameters in this simulation without the necessity of the machine itself. With this flexibility, each of the SPECT gamma cameras optimal properties could be investigated in a shorter time in comparison with using real SPECT device studies.

REFERENCES

1. Sung, J. Y., "Parathyroid ultrasonography: the evolving role of the radiologist," *Ultrasonography*, Vol. 34, no. 4, p. 268, 2015.
2. Mohebati, A., and A. Shaha, "Anatomy of thyroid and parathyroid glands and neurovascular relations," *Clinical Anatomy*, Vol. 25, no. 1, pp. 19–31, 2012.
3. Martin, W. H., M. P. Sandler, and M. D. Gross, "Thyroid, parathyroid, and adrenal gland imaging," in *Practical Nuclear Medicine*, pp. 247–272, Springer, 2005.
4. Hamidi, S., H. Koksall, O. Kurukahvecioglu, and F. Taneri, "Primary hyperparathyroidism due to parathyroid adenoma.," *Saudi Medical Journal*, Vol. 28, no. 2, pp. 305–306, 2007.
5. Reeve, T. S., B. H. Barraclough, L. W. Delbridge, B. G. Robinson, P. Clifton-Bligh, M. S. Sywak, and G. H. Fick, "Increase in presentations and procedure rates for hyperparathyroidism in northern sydney and new south wales," *The Medical Journal of Australia*, Vol. 177, no. 5, pp. 246–249, 2002.
6. Lundstroem, A. K., W. Trolle, C. H. Soerensen, and P. S. Myschetzky, "Preoperative localization of hyperfunctioning parathyroid glands with 4d-ct," *European Archives of Oto-Rhino-Laryngology*, Vol. 273, no. 5, pp. 1253–1259, 2016.
7. Tunninen, V., T. Kauppinen, and H. Eskola, "Optimization of 99m tc-sestamibi/123 i subtraction spect/ct protocol for parathyroid scintigraphy," in *EMBECE & NBC 2017*, pp. 847–851, Springer, 2017.
8. Holmberg, D., "Optimisation of image acquisition and reconstruction of 111in-pentetrotide spect," 2012.
9. Balta, S., and A. Guvenis, "Robust design of a breast scintigraphy collimator using monte carlo simulation and response surface method," in *European Journal of Nuclear Medicine and Molecular Imaging*, Vol. 34, pp. S165–S165, 2007.
10. Wong, K. K., L. M. Fig, M. D. Gross, and B. A. Dwamena, "Parathyroid adenoma localization with 99mtc-sestamibi spect/ct: a meta-analysis," *Nuclear Medicine Communications*, Vol. 36, no. 4, pp. 363–375, 2015.
11. Im, H.-J., I. K. Lee, J. C. Paeng, K. E. Lee, G. J. Cheon, K. W. Kang, J.-K. Chung, and D. S. Lee, "Functional evaluation of parathyroid adenoma using 99mtc-mibi parathyroid spect/ct: correlation with functional markers and disease severity," *Nuclear Medicine Communications*, Vol. 35, no. 6, pp. 649–654, 2014.
12. Kim, Y.-i., Y. H. Jung, K. T. Hwang, and H.-Y. Lee, "Efficacy of 99m tc-sestamibi spect/ct for minimally invasive parathyroidectomy: comparative study with 99m tc-sestamibi scintigraphy, spect, us and ct," *Annals of Nuclear Medicine*, Vol. 26, no. 10, pp. 804–810, 2012.
13. Krausz, Y., L. Bettman, L. Guralnik, G. Yosilevsky, Z. Keidar, R. Bar-Shalom, E. Even-Sapir, R. Chisin, and O. Israel, "Technetium-99m-mibi spect/ct in primary hyperparathyroidism," *World Journal of Surgery*, Vol. 30, no. 1, pp. 76–83, 2006.
14. Lavelly, W. C., S. Goetze, K. P. Friedman, J. P. Leal, Z. Zhang, E. Garret-Mayer, A. P. Dackiw, R. P. Tufano, M. A. Zeiger, and H. A. Ziessman, "Comparison of spect/ct, spect, and planar imaging with single-and dual-phase 99mtc-sestamibi parathyroid scintigraphy," *Journal of Nuclear Medicine*, Vol. 48, no. 7, pp. 1084–1089, 2007.

15. Ciappuccini, R., J. Morera, P. Pascal, J.-P. Rame, N. Heutte, N. Aide, E. Babin, Y. Reznik, and S. Bardet, "Dual-phase 99mTc sestamibi scintigraphy with neck and thorax spect/ct in primary hyperparathyroidism: a single-institution experience," *Clinical Nuclear Medicine*, Vol. 37, no. 3, pp. 223–228, 2012.
16. Martinez, D. A., D. R. King, C. Romshe, R. A. Lozano, J. D. Morris, M. S. O'Dorisio, and E. Martin, "Intraoperative identification of parathyroid gland pathology: a new approach," *Journal of Pediatric Surgery*, Vol. 30, no. 9, pp. 1306–1309, 1995.
17. Nichols, K. J., G. G. Tronco, and C. J. Palestro, "Effect of reconstruction algorithms on the accuracy of 99mTc sestamibi spect/ct parathyroid imaging," *American Journal of Nuclear Medicine and Molecular Imaging*, Vol. 5, no. 2, p. 195, 2015.
18. Mallak, N., A. Kashyap, J. Murguia, S. Sugg, and M. Graham, "Optimization of parathyroid imaging for small adenomas," *Journal of Nuclear Medicine*, Vol. 58, no. supplement 1, pp. 100–100, 2017.
19. Tunninen, V., T. Kauppinen, and H. Eskola, "Physical characteristics of collimators for dual-isotope imaging with 99mTc and 123I," in *EMBECE & NBC 2017*, pp. 245–249, Springer, 2017.
20. Tunninen, V., P. Varjo, J. Schildt, A. Ahonen, T. Kauppinen, I. Lisinen, A. Holm, H. Eskola, and M. Seppanen, "Comparison of five parathyroid scintigraphic protocols," *International Journal of Molecular Imaging*, Vol. 2013, 2013.
21. Council, N. R., *et al.*, *Advancing nuclear medicine through innovation*, National Academies Press, 2007.
22. Cherry, S. R., J. A. Sorenson, and M. E. Phelps, *Physics in nuclear medicine e-Book*, Elsevier Health Sciences, 2012.
23. Madsen, M. T., "Recent advances in spect imaging," *Journal of Nuclear Medicine*, Vol. 48, no. 4, pp. 661–673, 2007.
24. Hutton, B. F., "The origins of spect and spect/ct," *European Journal of Nuclear Medicine and Molecular Imaging*, Vol. 41, no. 1, pp. 3–16, 2014.
25. Cao, Z., C. Maunoury, C. C. Chen, and L. E. Holder, "Comparison of continuous step-and-shoot versus step-and-shoot acquisition spect," *The Journal of Nuclear Medicine*, Vol. 37, no. 12, p. 2037, 1996.
26. Wiczcerek, H., "The image quality of fbp and mlem reconstruction," *Physics in Medicine & Biology*, Vol. 55, no. 11, p. 3161, 2010.
27. Do, C. B., and S. Batzoglou, "What is the expectation maximization algorithm?," *Nature Biotechnology*, Vol. 26, no. 8, p. 897, 2008.
28. Conti, M., and M. E. Casey, "Estimating the optimal iteration number in iterative reconstruction: A statistical approach," in *Nuclear Science Symposium Conference Record, 2007. NSS'07. IEEE*, Vol. 6, pp. 4389–4394, IEEE, 2007.
29. Alessio, A., P. Kinahan, *et al.*, "Pet image reconstruction," *Nuclear Medicine*, Vol. 1, pp. 1–22, 2006.
30. Mettler, F. A., and M. J. Guiberteau, *Essentials of Nuclear Medicine Imaging E-Book*, Elsevier Health Sciences, 2011.

31. Barrack, F., J. Scuffham, and S. McQuaid, "Septal penetration correction in i-131 imaging following thyroid cancer treatment," *Physics in Medicine & Biology*, Vol. 63, no. 7, p. 075012, 2018.
32. tot Nederveen, W. H. d. V., B. L. van Eck-Smit, E. K. Pauwels, *et al.*, "Scatter correction on its own increases image contrast in ti-201 myocardium perfusion scintigraphy, but does it also improve diagnostic accuracy?," *Annals of Nuclear Medicine*, Vol. 17, no. 8, pp. 725–731, 2003.
33. Ashoor, M., A. Asgari, A. Khorshidi, and A. Rezaei, "Evaluation of compton attenuation and photoelectric absorption coefficients by convolution of scattering and primary functions and counts ratio on energy spectra," *Indian Journal of Nuclear Medicine: IJNM: the Official Journal of the Society of Nuclear Medicine, India*, Vol. 30, no. 3, p. 239, 2015.
34. Greenspan, B. S., G. Dillehay, C. Intenzo, W. C. Lavelly, M. O'Doherty, C. J. Palestro, W. Scheve, M. G. Stabin, D. Sylvestros, and M. Tulchinsky, "Snm practice guideline for parathyroid scintigraphy 4.0," *Journal of Nuclear Medicine Technology*, Vol. 40, no. 2, pp. 111–118, 2012.
35. Hindié, E., Ö. Ugur, D. Fuster, M. ODoherty, G. Grassetto, P. Ureña, A. Kettle, S. A. Gulec, F. Pons, and D. Rubello, "2009 eanm parathyroid guidelines," *European Journal of Nuclear Medicine and Molecular Imaging*, Vol. 36, no. 7, pp. 1201–1216, 2009.
36. Wijaya, I., "Chronic hypoparathyroidism due to partial thyroidectomy with intracranial calcification," *Acta Medica Indonesiana*, Vol. 48, no. 1, pp. 68–69, 2016.
37. Kunstman, J. W., J. D. Kirsch, A. Mahajan, and R. Udelsman, "Parathyroid localization and implications for clinical management," *The Journal of Clinical Endocrinology & Metabolism*, Vol. 98, no. 3, pp. 902–912, 2013.
38. Alenezi, S. A., S. M. Asa'ad, and A. H. Elgazzar, "Scintigraphic parathyroid imaging: Concepts and new developments," *Research and Reports in Nuclear Medicine*, Vol. 5, pp. 9–18, 2015.
39. Slater, A., and F. V. Gleeson, "Increased sensitivity and confidence of spect over planar imaging in dual-phase sestamibi for parathyroid adenoma detection," *Clinical Nuclear Medicine*, Vol. 30, no. 1, pp. 1–3, 2005.
40. Moka, D., E. Voth, M. Dietlein, A. Larena-Avellaneda, and H. Schicha, "Technetium 99m-mibi-spect: a highly sensitive diagnostic tool for localization of parathyroid adenomas," *Surgery*, Vol. 128, no. 1, pp. 29–35, 2000.
41. Öksüz, M. Ö., H. Dittmann, C. Wicke, K. Müssig, R. Bares, C. Pfannenber, and S. M. Eschmann, "Accuracy of parathyroid imaging: a comparison of planar scintigraphy, spect, spect-ct, and c-11 methionine pet for the detection of parathyroid adenomas and glandular hyperplasia," *Diagnostic and Interventional Radiology*, Vol. 17, no. 4, p. 297, 2011.
42. Islamian, J. P., A. Azazrm, B. Mahmoudian, and E. Gharapapagh, "Advances in pinhole and multi-pinhole collimators for single photon emission computed tomography imaging," *World Journal of Nuclear Medicine*, Vol. 14, no. 1, p. 3, 2015.
43. Klingensmith, W. C., P. J. Koo, A. Summerlin, B. W. Fehrenbach, R. Karki, B. C. Shulman, C. D. Raeburn, and R. C. McIntyre, "Parathyroid imaging: the importance of pinhole collimation with both single-and dual-tracer acquisition," *Journal of Nuclear Medicine Technology*, pp. jnmt-112, 2013.

44. Ljungberg, M., S.-E. Strand, and M. A. King, *Monte Carlo calculations in nuclear medicine: Applications in diagnostic imaging*, CRC Press, 2012.
45. Zubal, I. G., C. R. Harrell, E. O. Smith, Z. Rattner, G. Gindi, and P. B. Hoffer, "Computerized three-dimensional segmented human anatomy," *Medical Physics*, Vol. 21, no. 2, pp. 299–302, 1994.
46. Ljungberg, M., "The simind monte carlo program manual," 2017. Available : http://www2.msf.lu.se/simind/download/Simind_manual.pdf.
47. "Siemens symbia t series system specifications," 2013. Available : <https://3.imimg.com/data3/AC/PC/MY-13438971/gamma-camera.pdf>.
48. "General electric infinia hawkeye gamma camera system specifications," 2006. Available : <http://www.gammasys.com.ar/descargas/GE%20Infinia%20brochure%20data%20sheet.pdf>.
49. Kortelainen, M. J., T. M. Koivumäki, M. J. Vauhkonen, and M. A. Hakulinen, "Dependence of left ventricular functional parameters on image acquisition time in cardiac-gated myocardial perfusion spect," *Journal of Nuclear Cardiology*, Vol. 22, no. 4, pp. 643–651, 2015.
50. Beijst, C., J. W. Kist, M. Elschot, M. A. Viergever, O. S. Hoekstra, B. de Keizer, H. De Jong, *et al.*, "Quantitative comparison of 124i pet/ct and 131i spect/ct detectability," *J Nucl Med*, Vol. 57, pp. 103–108, 2016.
51. Zoccarato, O., D. Lizio, A. Savi, L. Indovina, C. Scabbio, L. Leva, A. Del Sole, C. Marcassa, Matheoud, *et al.*, "Comparative analysis of cadmium-zincum-telluride cameras dedicated to myocardial perfusion spect: A phantom study," *Journal of Nuclear Cardiology*, Vol. 23, no. 4, pp. 885–893, 2016.
52. Park, S. J., C.-L. Lee, H.-M. Cho, and H.-J. Kim, "Ultra high resolution spect with cdte for small animal imaging applications: Monte carlo simulation study using voxelized phantom," in *Nuclear Science Symposium and Medical Imaging Conference (NSS/MIC), 2011 IEEE*, pp. 3030–3033, IEEE, 2011.
53. Sabondjian, E., A. J. Mitchell, G. Wisenberg, J. White, K. J. Blackwood, J. Sykes, L. Deans, R. Z. Stodilka, and F. S. Prato, "Hybrid spect/cardiac-gated first-pass perfusion ct: locating transplanted cells relative to infarcted myocardial targets," *Contrast Media & Molecular Imaging*, Vol. 7, no. 1, pp. 76–84, 2012.
54. Chen, H., R. S. Sippel, and S. Schaefer, "The effectiveness of radioguided parathyroidectomy in patients with negative technetium tc 99m-sestamibi scans," *Archives of Surgery*, Vol. 144, no. 7, pp. 643–648, 2009.
55. Cardinale, J., "Poisson noise, an imagej plugin," 2010. Available: https://mosaic.mpi-cbg.de/Downloads/PoissonNoise_manual.pdf.